

# Multiple contact compression tests on sand particles.

M.C. Todisco<sup>+</sup>, W. Wang<sup>+</sup>, M.R.Coop<sup>\*</sup> and K. Senetakis<sup>#</sup>

## ABSTRACT

Particle crushing has been recognised to be of key importance for many engineering applications. In soil mechanics, this phenomenon has become crucial in defining a complete framework able to describe the mechanical behaviour of sands. In this study, the effect of multiple discrete contacts on the breakage of a grain was investigated, crushing coarse grains of a quartz sand and a crushed limestone sand between a number of support particles, thereby varying the number of contacts, i.e. the coordination number. The stress at failure was calculated when the particle broke, which was through a number of distinct modes, by chipping, splitting or fragmenting which were observed with the use of high speed microscope camera. The Weibull criterion was applied to calculate the probability of surviving grain crushing and the fracture modes were observed for each configuration of the supporting particles. The data showed that in addition to the number of the contacts the nature of those contacts, controlled by the particle morphology and mineralogy, play a significant role in determining the strength of a particle. The sphericity affected the strength for the softer limestone while the local roundness at the contacts was important for the harder quartz sand. Catastrophic explosive failure was more often observed in particles with harder contacts while softer contacts tended to mould relative to their neighbouring particles inducing a more frequent ductile mode of crushing.

<sup>+</sup> City University of Hong Kong

<sup>\*</sup> University College London, formerly City University of Hong Kong

<sup>#</sup> University of New South Wales, formerly City University of Hong Kong

## 26 1. INTRODUCTION

27 Understanding particle crushing is very important for modelling, simulation and optimisation  
28 of mineral and powder processing (Tavares, 2007) and in soil mechanics, establishing a link  
29 between particle breakage phenomena and the macro-mechanical behaviour of sands has  
30 become of key importance (McDowell and Bolton 1998; McDowell, 2002; Coop et al., 2004;  
31 Muir Wood, 2008; Altuhafi and Coop, 2011). Failure models accounting for the coordination  
32 number, CN, in an assembly of grains have been developed by many authors, for example  
33 Tsoungui et al. (1999) and Ben-Nun and Einav (2010) among others. In an assembly of poly-  
34 dispersed granular materials, the breaking process of the soil matrix depends on the strength  
35 of each grain, which varies with their size, and on the number of contacts which is established  
36 between grains, since the forces transferred within the assembly vary with the number of  
37 contact points. Contact force networks inside an assembly of discs have been determined by  
38 the use of photo-elasticity techniques (Drescher and De Josselin de Jong, 1972; Durelli and  
39 Wu, 1984). However, it is difficult to define the stress evolution in a system of sand  
40 specimens since the photo-elasticity method cannot be applied to sand particles, although  
41 Fonseca et al. (2016) have inferred the strong force network from an analysis of particle  
42 contacts with x-ray CT. Numerical simulations have explored the stress distributions which  
43 lead to the failure of an individual grain subjected to a system of forces within an assembly  
44 (Ben-Nun and Einav, 2010; Minh and Cheng, 2013). Gundepudi et al. (1997) extended the  
45 solution for the stress distribution in an elastic sphere under a single contact load (Dean et al.,  
46 1952) to spheres under multiple contacts. Numerically they found that the maximum stress  
47 away from the contact region was similar for uniaxial and four-point loading on different  
48 planes of the sphere, larger for three-point in-plane loading but smaller for six contact points.  
49 However, they also observed experimentally that the failure of glass and aluminium spheres  
50 initiated in the proximity of the contacts, where the contact forces reached the maximum.

51 In rock engineering, the Brazilian test has been used to assess indirectly the tensile strength of  
52 brittle materials. Li and Wong (2013) reviewed the mechanism of crack initiation inside the  
53 disc of rock. They found numerically that a crack in a disc subjected to two opposing forces  
54 might originate near to the two loading points along the central axis when the tensile strain  
55 overcomes a critical tensile strain threshold, or at the centre of the contact when the tensile  
56 stress overcomes the critical tensile stress threshold. However, if a fracture initiates far from  
57 the centre of the disc, the Brazilian test is not appropriate to measure the tensile strength of  
58 rocks (Fairhurst, 1964). For point load tests on an elastic sphere, Russell and Muir Wood

59 (2009) gave an analytical solution that showed the initial failure would occur just below the  
60 contact point and it was of shearing type, the failure criterion being dependent on the second  
61 invariant of the stress tensor. Russell et al. (2009) applied the same failure criterion to  
62 particles subjected to multi-contact loading within several different regular packings of  
63 spheres. The failure initiated near the largest contact force, when the ratio of the second to the  
64 first invariant of the stress tensor was the largest of the localised maxima, independently of  
65 the material properties or particle size. However, the yield or failure of the assembly would  
66 depend on both the maximum contact forces and the assembly stability.

67 Based on CT images, Zhao et al. (2015) were able to relate the internal features of quartz and  
68 decomposed granite particles to their geological origins and to explore how these features  
69 affected their mode of crushing. The single-particle crushing tests on quartz grains showed  
70 that the crushing occurred along tensile planes roughly parallel to the loading direction,  
71 although conchoidal in shape. However, they also observed an extensive fragmentation at the  
72 contact points as also shown by Gundepudi et al. (1997), which might have been generated  
73 by shear failure, as described by Russell and Muir Wood (2009).

74 This experimental study is an extension of preliminary results by Todisco et al. (2015) who  
75 performed multiple but discrete contact crushing tests on 60 particles of a crushed limestone  
76 and 68 of a quartz sand from the UK. The updated testing programme comprises 362 and 233  
77 tests on quartz and crushed limestone, respectively, the much larger number of tests allowing  
78 a much clearer assessment of the factors affecting the breakage. The data were interpreted in  
79 terms of nominal stresses, i.e. characteristic stresses, which might not reproduce accurately  
80 the real stress distributions within particles under compressive loads but they offer the basis  
81 for a statistical comparison between the different types of compressive loading. Specimens  
82 were tested varying the number of contact forces on the particles, i.e. the coordination  
83 number, CN. The stress at failure was calculated when the particle broke, which was through  
84 a number of distinct modes, by chipping, splitting or fragmenting. The Weibull criterion  
85 (Weibull, 1951) was applied to calculate the probability of surviving grain crushing and the  
86 influences of the particle morphology and mineralogy on failure were investigated.

87

## 88 2. MATERIALS, EQUIPMENT AND TESTING PROCEDURES

89

90 The crushing tests were performed at a constant rate of 0.1 mm/min in a modified CBR  
91 apparatus equipped with a high speed camera with a microscope lens of maximum  
92 magnification of 16x (Fig. 1). The fastest frame rate of the camera was 2130 frames/sec,  
93 however tests were conducted at 1000 frames/sec because this gave the best compromise  
94 between capturing time and exposure and so the best picture quality (Wang and Coop, 2016).  
95 The forces and displacements were measured with a load cell of 1000 N capacity and 0.1 N  
96 resolution and an LVDT of  $\pm 3.5$  mm linear range and 1  $\mu$ m resolution. The crushed particle,  
97 No.1 on Fig. 2, was placed in between others, which in turn were glued onto steel mounts  
98 using epoxy resin. The mounts were fixed into brass wells; the lower of the two was fixed to  
99 an aluminium platen which in turn was placed onto ball bearings in order to release the lateral  
100 restraint and ensure that the exact number of loading contacts occurred between the crushed  
101 particle and the others.

102 Wang and Coop (2016) investigated single particle crushing also using high speed  
103 photography, but here the aim of the work was to investigate the effects of the number and  
104 nature of the contacts. This photographic technique allows much larger numbers of particles  
105 to be tested than CT scanning, so that strength distributions may be determined. The tests  
106 were performed in three different configurations, varying the number of the contacts, CN,  
107 between the crushed particle and the others. The three different modes of the tests are  
108 described in Fig. 2. When the particle is crushed in between two hardened steel mounts, the  
109 test is the standard single particle crushing test (Nakata et al., 1999); when the particle is  
110 crushed between three particles at the bottom and one at the top, the test defines a multi-  
111 particle crushing test with CN equal to 4, while, when there are three particles at both the  
112 bottom and the top, the multi-particle crushing test has a CN equal to 6. It is emphasised that  
113 in the SP test an irregular sand particle has at least three points of contact if at rest on a  
114 horizontal plane and four if is crushed between flat surfaces. However, the configurations SP  
115 and CN4 of this paper are likely to be different because the contacts of the former would be  
116 in closer proximity. The single particle crushing tests have therefore been identified with SP.  
117 The differences of strength between the two types of test will be discussed below. The test  
118 configurations used are the only ones available for which the number of contacts can be  
119 ensured. While Russell et al. (2009) could investigate numerically the behaviour of particles  
120 within regular arrays of perfect equal sized spheres, these packings cannot be used in  
121 experimental work on real particles.

122 The coordination number, CN, and the type of support particles (steel balls, BP, or sand  
123 particles, PP) define the type of test. For example, CN4-BP refers to a test with steel ball  
124 support particles and a coordination number of 4. If sand particles were used for the support,  
125 they were always of the same size and mineralogy as that being crushed. It was rare that  
126 significant damage occurred to the support particles, and for the few occasions where it did  
127 happen the tests were discarded.

128 The crushing mechanism was investigated for two types of sands. The first material was the  
129 Leighton Buzzard sand (LBS), a quartz sand from the UK extensively studied in the  
130 geotechnical field since the early 70s (Stroud, 1971). The second sand was a crushed  
131 limestone (LMS) from China made of weak and angular calcite particles. The crushed  
132 limestone is a diagenetic rock, consolidated (compressed) to large stress levels and so is  
133 unlikely to have significant intra-particle voids or internal defects, as, for example, biogenic  
134 sands or weathered soils would show. Zhao et al. (2015) made CT scans of the LBS and also  
135 highly decomposed granite (HDG) particles to relate the initial microstructure to the fracture  
136 mechanism. The LBS particles only showed very few internal voids which did not influence  
137 the fracture pattern and the particles crushed with conchoidal fractures, as expected in quartz.  
138 In contrast, the complex initial microstructure of HDG, with intra-particle fissures, phase  
139 boundaries between different minerals and cleavage in some of those minerals, meant that the  
140 fracture patterns were dominated by the internal particle structure, with the coexistence of  
141 bending, shear and tensile cracks along different features. Wang and Coop (2016) also used  
142 decomposed granite and the LBS in their single particle tests. However, the complexity of the  
143 internal structure of the decomposed granite revealed by Zhao et al. meant that it was less  
144 suitable for the current study that was aimed at investigating the influence on breakage of the  
145 nature and number of contacts, which was why the crushed limestone was chosen instead as  
146 the second, softer and weaker material.

147 The three descriptor diameters were defined for the particles in their at-rest position as the  
148 maximum and intermediate Feret diameters in the horizontal plane and the minimum in the  
149 vertical, measuring each with a Vernier calliper of 0.01 mm resolution. The use of a Vernier  
150 calliper was preferred to a digital image method for the measurements of the particle  
151 dimensions because it allowed the characterisation of the large number of specimens required  
152 for the statistical analysis in a relatively short time but without jeopardising the measurement  
153 accuracy. The average of the minimum diameter, i.e. the thickness of the particle, was around  
154 2.20 mm for both the sands. The descriptor diameters along with the shape characteristics and

155 the global hardness of the materials are indicated in Table 1. The shape descriptors were  
 156 evaluated as sphericity,  $S$ , and roundness, although in this study, it was preferred to use a  
 157 local roundness parameter, in terms of the geometry of the grains at the contact rather than  
 158 the global roundness of the grains. The sphericity,  $S$ , was calculated from the two vertical  
 159 side views as the ratio between the radii of the maximum inscribed and the minimum  
 160 circumscribed circles defined from the outline of the particle (Krumbein and Sloss, 1963).  
 161 The side views were obtained from high quality images in two orthogonal directions. The  
 162 formula, which accounts for the average sphericity from both side views, is given in Eq. 1:

$$163 \quad S = \sqrt{S_A S_B} = \sqrt{\frac{r_{max,inc,A}}{r_{min,circ,A}} \cdot \frac{r_{max,inc,B}}{r_{min,circ,B}}} \quad (1)$$

164 where A and B refer to the different side views,  $S$  is the sphericity,  $r_{max,inc}$  is the maximum  
 165 inscribed radius and  $r_{min,circ}$  is the minimum circumscribed radius.

166 A new parameter, named relative local roundness,  $r_{rl}$ , was defined to quantify the local  
 167 outlines of two particles at their contacts. An image processing technique was used both in  
 168 the quantification of this and the sphericity. The pictures of the particles were first  
 169 transformed into a binary format and then, for  $r_{rl}$ , a polynomial function  $f(x)$  of the fifth order  
 170 was used to fit the outline of the binary image using Matlab. The fifth order function was the  
 171 best fit of the particle outlines. Fig. 3 shows a comparison between a typical particle outline  
 172 and the fitting quality of the polynomial functions of different orders. At the high  
 173 magnification shown, the pixel size of the captured image is evident but it is clear that  
 174 functions of lower degrees are too inaccurate to characterise the local curvature, while the  
 175 sixth order did not show a better accuracy. The whole particle perimeter was divided in two  
 176 parts so that the digitised outline was only a function of one independent variable ( $x$ ). The  
 177 radius of curvature  $r_i(x)$  of one contact point was calculated according to the general formula  
 178 for the curvature,  $\chi$ , of a given function,  $f(x)$ :

$$179 \quad \chi = \frac{1}{r_i(x)} = \frac{|f(x)''|}{(1+(f(x)')^2)^{3/2}} \quad (2)$$

180 where  $f(x)$  is the function at the point ( $x$ ) selected on the contact surfaces. The radius of  
 181 curvature of each particle  $r_j$  was calculated as the average of  $r_i(x)$  along the whole contact  
 182 region:

$$183 \quad r_j = \sum_{i=1}^N \frac{r_i(x)}{N} \quad (3)$$

184 where N is the number of points that defined the function  $f(x)$  along the contact region. Since  
 185 the test configuration meant that the crushed particle was in contact with others, a measure of  
 186 the geometry for each contact was established as follows (Eq. 4):

$$187 \quad r_{1,j} = \frac{r_1 r_j}{r_1 + r_j} \quad (4)$$

188 where 1 refers to the crushed particle and j to the j-th particle which was in contact with  
 189 particle 1. The  $r_{rl}$  was then defined as the minimum  $r_{1,j}$  divided by the thickness of the  
 190 crushed particle,  $d_{1,min}$ , in order to create a parameter independent of the particle size (Eq. 5).  
 191 The procedure for the calculation of the shape descriptors is shown in detail in Fig. 4, where  
 192 the functions  $f(x)$  are schematised as arcs and only three views are presented for simplicity  
 193 (arcs were not used in the actual calculations).

$$194 \quad r_{rl} = \frac{\min(r_{1,j})}{d_{1,min}} \quad (5)$$

195 The calculation of  $r_{rl}$  may be conducted in 2-D or 3-D. In 3-D, the contacts were not assessed  
 196 only from the front view but different orientations were considered in order to give the  
 197 optimum and complete view of the contacts. For example, generally, five pictures were taken  
 198 for each CN4 configuration (three at the bottom and two at the top). Wang and Coop (2016)  
 199 conducted only single-particle crushing tests, but demonstrated that there was no significant  
 200 difference between using a 2-D or 3-D parameter. Ideally the contact geometry could be  
 201 quantified most accurately using CT scanning, (e.g. Fonseca et al., 2013), but it would be  
 202 impractical to scan a sufficient number of tests to be able to establish the characteristic  
 203 stress: survival probability curves.

204 The high-speed camera was used to record the crushing process during the test. The videos  
 205 were post-processed in order to locate the initiation of the failure crack within the particle and  
 206 characterize the crushing mechanism. The Weibull criterion was applied to the data analysis  
 207 and the failure stresses were obtained from Eq. 6, which assumes a tensile failure:

$$208 \quad \sigma_f = \frac{F}{\pi \left(\frac{d_{int}}{2}\right) \left(\frac{d_{min}}{2}\right)} \quad (6)$$

209 where F is the maximum force recorded from the test, and  $d_{int}$  and  $d_{min}$  are the intermediate  
 210 and minimum diameters of the crushed particle, respectively. Considering the failure area of  
 211 the particle as the geometric mean of the  $d_{int}$  and  $d_{min}$  diameters would allow the effect of the

212 particle morphology to be accounted for, especially in the case of the elongated particles. An  
 213 example of the effect of the failure area on the particle strength is shown in Fig. 5 where three  
 214 different survival probabilities obtained from the geometric mean area (present study), the  
 215 circle area (Nakata et al., 1999) and the circle area increased by a factor of 1.1, as adopted by  
 216 Hiramatsu and Oka (1966), are compared. The use of Eq. 6 implies a simplistic stress regime  
 217 within the particles at failure that is undoubtedly far from reality, particularly for the CN4 and  
 218 CN6 tests, yet it is probably preferable as a means of comparison to using the failure forces,  
 219 although the conclusions would be the same whether the analysis was in terms of force or  
 220 stress. The calculation of the characteristic stress is based on the total force acting on the  
 221 system, which must all be transmitted through the central crushed particle, although of course  
 222 the local contact forces will be lower for a higher CN.

223 Todisco et al. (2015) observed different contact behaviours between quartz and calcite grains  
 224 and underlined that the hardness of particles at the contacts was an important factor in  
 225 characterising the crushing mechanism. However, they based their relationship on generic  
 226 mineral hardness values available in the literature. The micro-hardnesses of LBS and LMS  
 227 grains have now been measured in order to describe in a more accurate way the contact  
 228 properties. A Fisherscope HM2000XYp was used on fresh particle surfaces with an  
 229 indentation force of 1N for both the materials. Polishing and grinding the particle surfaces  
 230 were avoided since these actions may affect the residual stress state and so the hardness  
 231 (Griepentrog et al., 2002). The micro-hardness values reported in Table 1 refer to Martens  
 232 hardness (HM) which is the ratio between the maximum specified force  $F$  and the surface  
 233 area  $A(h)$  of the Vickers indenter penetrating from the zero-point of the contact:

$$234 \quad HM = \frac{F}{A(h)} = \frac{F}{h^2 \frac{4\sin(\frac{\alpha}{2})}{\cos^2(\frac{\alpha}{2})}} \quad (7)$$

235 where  $\alpha$  is the angle between the two opposite faces of the Vickers indenter and  $h$  is the depth  
 236 of the indentation. Several specimens of LBS and LMS were glued with resin epoxy on to a  
 237 steel mount and by means of a microscope, the flattest surfaces of each were indented at three  
 238 different locations. The average value of HM for the LBS grains was equal to 6.2 GPa and of  
 239 LMS 1.6 GPa.

### 240 3. RESULTS

241



242 Weibull statistics are presented for both the LMS and LBS particles along with the m-moduli,  
243 but the effect of the geometry of the contacts on the crushing mechanism is examined only  
244 for the LBS particles. It was not possible to calculate the local relative roundness of the LMS  
245 particles due to the geometry of the contacts, which often consisted of flat-to-flat surfaces  
246 (Fig. 6). In contrast, accurate values of  $r_{rl}$  could be calculated from the geometry of the  
247 contacts of the LBS particles. The total number of tests and the number of those used for the  
248 study of morphology are indicated in Table 2. Within the study of the effects of morphology,  
249 those tests that showed incipient cracks at the top of the crushed particle and also the number  
250 of tests that have not been considered in a more detailed analysis of morphology are  
251 highlighted.

252

### 253 *3.1 Effects of the particle morphology and hardness*

254

255 In order to take into account the particle sphericity, the tests on the LMS particles were  
256 divided into two groups. The first group was used to determine the probability of survival of  
257 particles characterised by values of sphericity ranging between 0.5 and 0.7, while the second  
258 probability curve was generated for the more spherical particles. Similar trends could be  
259 identified for both the CN4-PP and CN6-PP tests as presented in Fig. 7, where the more  
260 spherical particles appear to be generally weaker. However, for very weak particles ( $\sigma_f$  less  
261 than 10MPa) the trend is reversed. Unland and Al-Khasawneh (2009) investigated the  
262 influence of the shape of limestone particles in impact crushing tests and they found that less  
263 spherical particles were stronger.

264 The same selection was applied to the LBS specimens, for which the sphericity ranges chosen  
265 were between 0.4-0.6 or 0.6-0.8 for the CN4 tests and 0.5-0.7 or 0.7-0.9 for the CN6. In  
266 contrast to the LMS behaviour, the data for the LBS particles show that the sphericity has no  
267 clear effect on the failure stress, as shown in Fig. 8. For the LBS the effect of the relative  
268 local roundness at the contacts,  $r_{rl}$ , was evaluated by dividing the data into three groups of  $r_{rl}$   
269 = 0.2-0.4, 0.4-0.5 and 0.5-0.7. The results show that particles with lower  $r_{rl}$ , i.e. sharper  
270 contacts, are weaker than particles showing more rounded contact geometries (Fig. 9).

271 It might be inferred that for stronger particles, like the LBS, the geometry of the contacts  
272 dominates the crushing mechanism, obscuring the effect of the overall particle shape. When

273 the contacts are sharp, i.e. lower  $r_{i1}$ , the particle experiences large stress concentrations at the  
274 contacts which may lead to a crack initiation in the proximity of the sharp contact before the  
275 stresses can redistribute inside the whole particle. On the contrary, soft particles do not  
276 experience any stress concentration at the contacts because they mould relative to the  
277 neighbouring particles and so the whole particle participates in the crushing process. An  
278 example of this inference is shown for the LMS in Fig. 10 where, as loading proceeds, the  
279 displacements are large, but there is no evident overall failure initially, and instead it seems  
280 that the contacts deform substantially, to the point where the central particle starts to be  
281 obscured. This phenomenon must be associated more with the hardness of the limestone than  
282 its stiffness since the Young's modulus of calcite is 73–84 GPa, while that of quartz is only  
283 slightly higher at 94–98 GPa (Mavko et al., 1998; Jaeger et al., 2007).

284 The influence of sphericity on the crushing of the LMS particles contradicts the work of  
285 Hiramatsu and Oka (1966) who found, both by means of photo-elasticity and experiments,  
286 that the stress field inside an irregular piece of rock may be considered as the same as that  
287 within a sphere and that the tensile stress in the rock, subjected to a pair of opposing forces,  
288 agreed well with that calculated for a sphere if the latter were reduced by a factor of 0.9.

289 In Fig. 11, the failure stress of LMS is related to that of LBS for the test configurations of  
290 CN6-PP and CN4-PP. Each data point represents the failure stress selected at the same  
291 survival probability value on the curves of LMS and LBS respectively, so that lower values  
292 of stress describe higher probabilities of survival. The gradient of this relationship is 0.30,  
293 which is similar to the ratio of the micro-hardnesses of the LBS and LMS particles. This  
294 result suggests that the micro-hardness may play a significant role through the deformation of  
295 the contacts.

296

### 297 *3.2 Effect of the support particles*

298 In Fig. 12, the survival probability curves for the CN6 configuration for the LBS clearly show  
299 that the particles crushed between steel balls are stronger than those crushed between  
300 particles but no significant difference can be observed between the two types for the CN4  
301 configuration. On the other hand, the LMS particles give similar survival probabilities for all  
302 the test configurations, as presented in Fig. 13. Indeed, the maximum variation between the  
303 characteristic stresses at a survival probability of 37% for LMS particles crushed in SP, CN4-  
304 BP and CN6-BP configurations was only 1 MPa. A small number of tests were also carried

305 out on smaller particles which show larger failure stresses than the larger particles, as  
306 expected (Nakata et al., 1999).

307 This dissimilarity may be attributed to the different natures of the contacts which are  
308 established between strong and soft particles. The geometry of the contacts of a quartz  
309 particle is preserved during the test and at the contacts large stress concentrations might occur  
310 as they transfer the load without changing their morphology significantly. When a quartz  
311 grain is compressed between 6 steel balls, each contact experiences less stress concentration  
312 than during loading between 4 or 2 points. On the other hand, the soft contacts of an LMS  
313 grain do not preserve their geometry during loading, moulding relative to the neighbouring  
314 contacts, hence the stress distribution may vary much less when the LMS grain is crushed  
315 between hard (steel balls) or soft (LMS particles) materials.

316

### 317 *3.3 Effect of coordination number*

318

319 The force-displacement curves of uniaxial compression tests (SP) and particle to particle tests  
320 (CN4 and CN6) for LBS and LMS are presented in Fig. 14 (the data for LMS are redrawn  
321 from Todisco et al., 2015). Test LBS-CN6-PP shows some stick-slip behaviour due to some  
322 small movement at the particle contacts. Generally, the increase of coordination number did  
323 not change the crushing behaviour of the quartz and limestone particles, as seen in these  
324 figures, or the failure mechanisms. The LBS particles showed brittle failure (the curves are  
325 monotonic and the displacements are small) with the development of conchoidal fractures,  
326 whereas the LMS particles failed in a ductile way reaching larger displacements and showing  
327 a saw-tooth shaped curve. It might be expected that the failure force should increase with the  
328 increase of the coordination number, and Fig. 14 already shows an example of this variation.  
329 For the LBS grains, the CN6 configuration leads to a larger failure force than CN4 or SP  
330 which are quite similar. This suggests that the location of the applied loads does not influence  
331 the particle strength for SP and CN4. The effect of the coordination number on the failure  
332 force of the LMS particles in Fig. 14 is less pronounced due to the soft nature of the contacts.

333 In Fig. 12 the effect of coordination number is quite clear for the quartz particles which are  
334 more prone to break when subjected to diametrically opposite forces (SP) than those  
335 subjected to a more complex system of forces (CN6). At the 37% probability, the

336 characteristic stress of particles crushed between two steel platens is generally lower (45  
 337 MPa) than that calculated for the particles crushed between other particles; for example, the  
 338 characteristic stress of LBS-CN6-PP is 51 MPa and that of LBS-CN6-BP 71 MPa. The CN4  
 339 configuration does not have a clear effect on the particle strength. This might be attributed to  
 340 the configuration of the loading points, where there are three contact points at the base and  
 341 one at the top, which may resemble more that of a single particle crushing test since in this  
 342 configuration the particle will always rest on three points at its base prior to the loading  
 343 process. Therefore, it might be difficult to see a net variation between the strength obtained  
 344 from the SP and CN4 tests.

345 For the LMS particles, as explained in Section 3.2, the effect of the coordination number is  
 346 less clear, as shown in Fig. 13, although the characteristic stresses for CN6-PP tests are still  
 347 slightly higher than for the other test configurations. The configuration CN4-BP overlaps that  
 348 of the single particle crushing test (SP) for probabilities larger than 60%. This underlines that  
 349 the location of the applied loads does not influence the particle strength also for soft particles.  
 350 The factor that accounts for the variability of strength within the population of particles is the  
 351 m-modulus, which is used to describe the uniformity of the strength  $\sigma$  of a population of  
 352 grains and increases with decreasing the variability of particle strength. It generally varied  
 353 from 2 to 5 for LMS and from 3.5 to 4.5 for LBS (Fig. 15), but no influence of the test  
 354 configuration could be found on the m-modulus.

355 Simplified failure criteria developed for a disc can be used to explain why a particle subjected  
 356 to diametrical forces is more prone to break than one subjected to a set of forces. Detailed  
 357 explanations are given in the failure models of Tsoungui et al. (1999) and Ben-Nun and Einav  
 358 (2010). When a grain is subjected to a complex state of stress, its stress condition can be  
 359 reduced to the state of principal stresses in the first order, which compress the particle by the  
 360 hydrostatic pressure,  $p$ , and the deviatoric stress,  $\tau$ . When the tensile stress becomes greater  
 361 than a threshold, a crack initiates at the disc centre and the grain fails by tensile splitting. The  
 362 expression given in Eq. 8 (Tsoungui et al., 1999) implies that a grain has a higher probability  
 363 of splitting when the deviatoric stress,  $2\tau$ , is much larger than the hydrostatic pressure,  $p$ , i.e.  
 364 when diametrical forces act on the particle:

$$365 \quad \sigma_{xx}^0 = 2\tau - p \geq \sigma_{crit}(R) \quad (8)$$

366 where  $\sigma_{xx}^0$  is the tensile stress acting at the disc centre and  $\sigma_{crit}(R)$  depends on the nature of  
 367 the material, the dimension of the grain and the Weibull modulus,  $m$ .

368 Another example of a failure criterion which considers the role of the coordination number is  
 369 that of Ben-Nun and Einav (2010). In their failure model of a grain subjected to isotropic  
 370 loading from neighbouring grains, they considered the possibility that the crack initiates  
 371 through in-plane shear fractures, i.e. mode II of Irwin's (1957) failure criteria. In this case,  
 372 the authors proposed a threshold of  $F_{crit}$  equal to:

$$373 \quad F_{crit} = d\sigma_{crit}f_w f_d f_{CN} \quad (9)$$

374 where  $d$  is the thickness of the grain,  $\sigma_{crit}$  is the tensile stress at failure for the largest particle,  
 375  $f_w$  is a factor accounting for particle imperfections,  $f_d$  is a factor considering the geometry of  
 376 the particle at the contacts and  $f_{CN}$  is a factor accounting for the effect of the coordination  
 377 number on the crushing mechanism. The expression for  $f_{CN}$ , as given by Ben-Nun and Einav  
 378 (2010) and shown in Eq. 10, implies that as the coordination number increases, the factor  
 379 increases leading to an increase of the critical stress threshold:

$$380 \quad f_{CN} = (CN - 1)e^{(D/d)(CN-2)(CN-3)/4CN} \quad (10)$$

381 where  $D$  is the diameter of the neighbouring particles,  $d$  is the dimension of the crushed  
 382 particle and  $CN$  is the coordination number of the crushed particle. From Eq. 9, an increase of  
 383  $F_{crit}$  is reflected as a decrease of probability of failure of a grain with a higher coordination  
 384 number.

385

### 386 *3.4 Characterization of the crushing mechanism*

387 The characteristic stresses calculated assume that the crushed particle failed in a tensile mode,  
 388 obeying Griffith's criterion, for which a crack initiates in the centre of a disc when it is  
 389 subjected to diametrical loads. Complete stress solutions for a grain that which fails in  
 390 tension under two opposite loads acting on a finite arc have been formulated by several  
 391 researchers, Hondros (1959) and Hiramatsu and Oka (1966) among others, and they are used  
 392 to calculate the tensile strength of a disc of rock in the Brazilian test (Eq. 11),

$$393 \quad \sigma = \frac{F}{\pi R t} \quad (11)$$

394 where the failure force ( $F$ ) acts on the disc over an arc not greater than  $10^\circ$  (Li and Wong,  
 395 2013) and  $R$  and  $t$  are the radius and the thickness of the disc, respectively.

396 It has been argued that this formula might not be suitable for the estimation of the tensile  
397 strengths of rocks because the crack does not initiate in the centre but near the loading point  
398 (Fairhurst, 1964; Li and Wong, 2013). Recently, Russell and Muir Wood (2009) formulated a  
399 model for a point loaded sphere in which the crack initiation occurs when the ratio between  
400 the second invariant of the deviatoric stress tensor,  $J_2$ , and the first invariant of the stress  
401 tensor,  $I_1$ , is a maximum, which is essentially a maximum ratio of shear to normal stress  
402 invariants. In their work, the location of the initial failure was near the point load, at a  
403 distance between 0.7-0.9 from the centre of the sphere. In this study, this possibility was  
404 considered by eliminating the tests which showed a failure at the top for CN4 and SP tests  
405 from the data, although they were small in number as indicated in Table 2. The videos were  
406 recorded with the high speed camera and the analysis was applied only to the LBS particles  
407 tested between steel platens (SP) or 4 other particles (CN4-PP). The CN6-PP configuration  
408 was not considered because in this case the crack initiation may occur anywhere within the  
409 particle, since the forces are more equally distributed around the grain. The LMS particles  
410 were not analysed because it was difficult to determine the initiation of the failure, because  
411 the large deformations at the contacts tended to obscure the central particle.

412 As indicated in Table 2, out of 76 SP particles only 8 showed a failure near the top contact.  
413 Failures near the base contact were not eliminated also for SP tests because the base contact  
414 should not be unique. Of the 14 CN4-PP tests discarded, 6 showed a failure near the top  
415 contact and the remaining 8 were not taken into account because the location of the initial  
416 failure was unclear. The new probability curves shift to the right showing a small increase of  
417 particle strength (Fig. 16). This is more evident for the tests carried out in the CN4  
418 configuration in which the characteristic stress increased from 45 MPa to 51 MPa, although a  
419 smaller number of tests was performed in comparison with the SP configuration. Any  
420 conclusion might be slightly speculative at this stage, because a large number of tests would  
421 be required to investigate whether this type of test is suitable to assess the tensile strength of  
422 the sand particles in multi-axial loading tests.

423 The mode of failure was also analysed through the high speed videos recorded during the  
424 tests. The two different sands behaved very differently as expected. The soft LMS crushed  
425 into many pieces in a ductile way, reaching ultimate failure by the progressive breakage of  
426 the asperities and large deformation of the contacts. Fig. 10 shows a sequence of the images  
427 captured during the video of the test and this was typical of all the tests. The crushing mode  
428 of the quartz grains was analysed for both the CN4- and CN6-PP tests. The brittle failure,

429 common for quartz, was divided into three categories: if a grain suddenly shattered into many  
430 tiny pieces, the crushing process was classified as fragmentation, while if the grain split in  
431 two or more large parts, the crushing process was classified as splitting. It was observed that  
432 some grains failed also by the chipping of a smaller part of the particle not involving the  
433 entire particle in the crushing process (defined as “abrasion” by Tsoungui et al., 1999).  
434 Markides et al. (2010) found that discontinuities of stress and displacement fields concentrate  
435 at the edges of the load contacts and so the crack might initiate from the perimeter of the  
436 specimen. If it is made of hard material, this might not allow a smooth transition of the crack  
437 from the edge through the less loaded part and therefore the failure occurs by chipping off a  
438 piece of the specimen and not by splitting or fragmentation.

439 The CN4-PP specimens involved all the three crushing categories; out of the 32 tests for  
440 which a video was available, 25% failed by fragmentation, 69% by splitting and 6% by  
441 chipping (Figs. 17-19). The particles of CN6-PP failed predominantly by splitting,  
442 maintaining the two or three pieces generated from the crushing in place. An example is  
443 given in Fig. 20. The confinement given by this test configuration might cause this  
444 phenomenon. This recalls the behaviour of sand grains in triaxial tests as observed by  
445 Bandini and Coop (2011) or oedometer tests by Bolton and Cheng (2002), in which a particle  
446 that breaks while it is surrounded by others tends to create fragments that are held in close  
447 proximity to each other after failure occurs, as shown Fig. 21.

#### 448 4. CONCLUSIONS

449 Many factors may be involved in the complex mechanisms of breakage of a sand grain. An  
450 analysis of the particle morphology and mineralogy, the nature, the geometry and the number  
451 of contacts was conducted through multi-contact compression tests on sand particles. It was  
452 found that the sphericity affects the strength for soft but not for hard materials, for which it  
453 seems to be obscured by the relative local roundness at the contacts. The more spherical of  
454 the limestone particles were stronger, and sharper contacts led to a decrease in the failure  
455 stress for quartz particles. Key importance in the crushing mechanism might be attributed to  
456 the material hardness which may affect the particle strength through the deformation of the  
457 contacts. The main difference between the crushing behaviour of quartz and calcite grains  
458 was therefore attributed to the nature of the contacts. Hard contacts preserve their  
459 morphology during loading, experiencing large stress concentrations prior to failure. Soft

460 contacts mould relative to their neighbouring particles, involving the entire particle in the  
461 crushing mechanism.

462 Generally, an increase of the number of contacts induced an increase of particle stress at  
463 failure. The assumption of a tensile failure was adopted to determine the Weibull probability  
464 of the populations of sand particles, but a much larger number of tests would be needed to  
465 assess whether this approach is suitable to calculate the tensile strength of sand particles,  
466 which would be highly time-consuming for these multiple contact tests.

467 If the coordination number was four, either in the CN=4 or SP tests, then failure occurred by  
468 splitting, fragmenting or chipping but for CN=6 generally only splitting occurred,  
469 maintaining the products of the crushing in place.

#### 470 5. ACKNOWLEDGEMENTS

471 The work described in this paper was fully supported by a grant from the Research Grants  
472 Council of the Hong Kong Special Administrative Region, China (Project No. CityU  
473 112712).

#### 474 6. REFERENCES

475 Altuhafi, F.N. and Coop, M.R., 2011. Changes to particle characteristics associated with the  
476 compression of sands. *Géotechnique*, 61(6), pp. 459-471.

477 Bandini, V. and Coop, M.R., 2011. The influence of particle breakage on the location of the  
478 critical state line of sands. *Soils and Foundations*, 51(4), pp. 591-600.

479 Ben-Nun, O. and Einav, I., 2010. The role of self-organization during confined comminution  
480 of granular materials. *Phil. Trans. R. Soc. A*, 368, pp. 231-247.

481 Bolton, M.D. and Cheng, Y.P., 2002. Micro-geomechanics. Lisse, Springman (ed.), pp. 59-  
482 69.

483 Coop, M.R., Sorensen, K.K., Bodas Freitas, T. and Georgoutsos, G., 2004. Particle breakage  
484 during shearing of a carbonate sand. *Géotechnique*, 54(3), pp. 157-163.

485 Dean, W.R., Sneddon, A. M. and Parsons, H.V., 1952. Distribution of stress in a decelerating  
486 elastic sphere. *Selected government research reports: Strength and testing of Materials: Part*  
487 *II: Testing methods and tests results*, HSMO, London, pp. 212-234.



488 Drescher, A. and De Josselin De Jong, G., 1972. Photoelasticity verification of a mechanical  
489 model for the flow of a granular material. *J. Mech. Phys. Solids*, 20(5), pp. 337-351.

490 Durelli, A.J. and Wu, D., 1984. Loads between disks in a system of discrete elements.  
491 *Experimental Mechanics*, 24(4), pp. 337-341.

492 Fairhurst, C., 1964. On the validity of the Brazilian test for brittle materials. *Int. J. Rock*  
493 *Mech. Min.*, 1, pp. 515-526.

494 Fonseca, J., Nadimi, S., Reyes-Aldasoro, C.C., O'Sullivan, C. and Coop, M.R., 2016. Image-  
495 based investigation into the primary fabric of stress transmitting particles in sands. *submitted*  
496 *to Soils and Foundations*.

497 Fonseca, J., O'Sullivan, C., Coop, M.R. and Lee, P.D., 2013. Quantifying the evolution of  
498 soil fabric during shearing using directional parameters. *Géotechnique*, 63(6), 487-499.

499 Griepentrog, M., Ullner, C., and Duck., A., 2002. Instrumented indentation test for hardness  
500 and materials parameter from millinewtons to kilonewtons. *11th IMEKO TC05 Conference*  
501 *on hardness measurement*, Celle, Germany, 24-26 September, pp. 53-58.

502 Gundepudi, M.K., Sankar, B.V., Mecholsky, J.J. and Clupper, D.C., 1997. Stress analysis of  
503 brittle spheres under multiaxial loading. *Powder Technology*, 94 (2), pp. 153-161.

504 Hiramatsu, Y. and Oka, Y., 1966. Determination of tensile strength of rock by compression  
505 test of an irregular test piece. *Int. J. Rock. Mech. Min.*, 3, pp. 89-99.

506 Hondros, G., 1959. The evaluation of Poisson's ratio and the modulus of materials of a low  
507 tensile resistance by the Brazilian (indirect) test with particular reference to concrete. *Aust. J.*  
508 *Appl. Sci.*, 10(3), pp. 243-268.

509 Irwin, G., 1957. Analysis of stresses and strains near the end of a crack traversing a plate. *J.*  
510 *Appl. Mech.*, 24, pp. 361-364.

511 Jaeger, J. C., Cook, N. G. W. and Zimmerman, R., 2007. *Fundamentals of rock mechanics*.  
512 4th ed. Oxford: Wiley-Blackwell.

513 Krumbein, W.C. and Sloss, L.L., 1963. Stratigraphy and sedimentation. San Francisco: W.H.  
514 Freeman and Company.

515 Li, D. and Wong, L.N.Y., 2013. The Brazilian disc test for rock mechanics applications:  
516 review and new insights. *Rock Mech. Rock. Eng.*, 46(2), pp. 269-287.

517 Markides, C.F., Pazis, D.N. and Kourkoulis, S.K., 2010. Closed full-field solutions for  
518 stresses and displacements in the Brazilian disk under distributed radial load. *Int. J. Rock*  
519 *Mech. Min. Sci.*, 47(2), pp. 227-237.

520 Mavko, G., Mukerji, T. and Dvorkin, J., 1998. *The rock physics handbook: tools for seismic*  
521 *analysis in porous media*. Cambridge: Cambridge University Press.

522 McDowell, G.R. and Bolton, M.D., 1998. On the micromechanics of crushable aggregates.  
523 *Géotechnique*, 48(5), pp. 667-679.

524 McDowell, G., 2002. On the yielding and plastic compression of sand. *Soils and*  
525 *Foundations*, 42(1), pp. 139-145.

526 Minh, N.H. and Cheng, Y.P., 2013. A DEM investigation of the effect of particle-size  
527 distribution on one-dimensional compression. *Géotechnique*, 63(1), pp. 44-53.

528 Muir Wood, D., 2008. *Critical state and soil modelling*. Amsterdam, The Netherlands, IOS  
529 Press, pp. 51-72.

530 Nakata, Y., Hyde, A.F.L., Hyodo, M. and Murata, H., 1999. A probabilistic approach to sand  
531 particle crushing in the triaxial test. *Géotechnique*, 49(5), pp. 567-583.

532 Russell, A.R. and Muir Wood, D., 2009. Point load tests and strength measurements for  
533 brittle spheres. *Int. J. Rock Mech. Min. Sci.*, 46(2), pp. 272-280.

534 Russell, A.R., Muir Wood, D. and Kikumoto, M. 2009. Crushing of particles in idealised  
535 granular assemblies. *J. Mech. Phys. Solids*, 57(8), pp. 1293-1313.

536 Stroud, M., 1971. *Sands at low stress levels in the S.S.A.*, s.l.: Cambridge University.

537 Tavares, L., 2007. *Breakage of single particle: quasi-static*. In: *Handbook of Powder*  
538 *Technology*-Volume 12. s.l.:Elsevier, pp. 3-68.

539 Todisco, M.C., Coop, M.R., Senetakis, K. and Guo, Q., 2015. The effect of coordination  
540 number on particle crushing. *Geomechanics from Macro to Micro, Proc. of the TC 105*  
541 *ISSMGE, IS-Cambridge 2015, Vol.2*, 1063-1068.

542 Tsoungui, O., Vallet, D. and Charmet, J.C., 1999. Numerical model of crushing of grains  
543 inside two-dimensional granular materials. *Powder technology*, 105(1), pp. 190-198.

544 Unland, G. and Al-Khasawneh, Y., 2009. The influence of particle shape on parameters of  
545 impact crushing. *Minerals Engineering*, 22(3), pp. 220-228.

546 Wang, W. and Coop, M.R., 2016. An investigation of breakage behaviour of single sand  
547 particles using a high-speed microscope camera. *Géotechnique*, DOI: [http://dx.doi.org/10.16](http://dx.doi.org/10.1680/jgeot.15.P.247)  
548 [80/jgeot.15.P.247](http://dx.doi.org/10.1680/jgeot.15.P.247).

549 Weibull, W., 1951. A statistical distribution function of wide applicability. *Journal of applied*  
550 *mechanics*, pp. 293-297.

551 Zhao, B., Wang, J., Coop, M., R., Viggiani, G. and Jiang, M., 2015. An investigation of  
552 single sand particle fracture using X-ray micro-tomography. *Géotechnique*, 65(8), pp. 625-  
553 641.

554

555

556

## 557 TABLES

558 Table 1 Characteristics of the LBS and LMS particles (dimensions in  $\mu\text{m}$ , micro-hardness,  
559 HM, in GPa).

MATERIAL	$d_{\text{max}}$	$d_{\text{int}}$	$d_{\text{min}}$	S	$r_{\text{rl}}$	HM
LBS	3.61	2.90	2.21	0.63	0.48	6.2
LBS	2.62	2.15	1.62	-	-	6.2
LMS	3.46	2.70	2.24	0.69	-	1.6
LMS	2.41	1.86	1.51	-	-	1.6

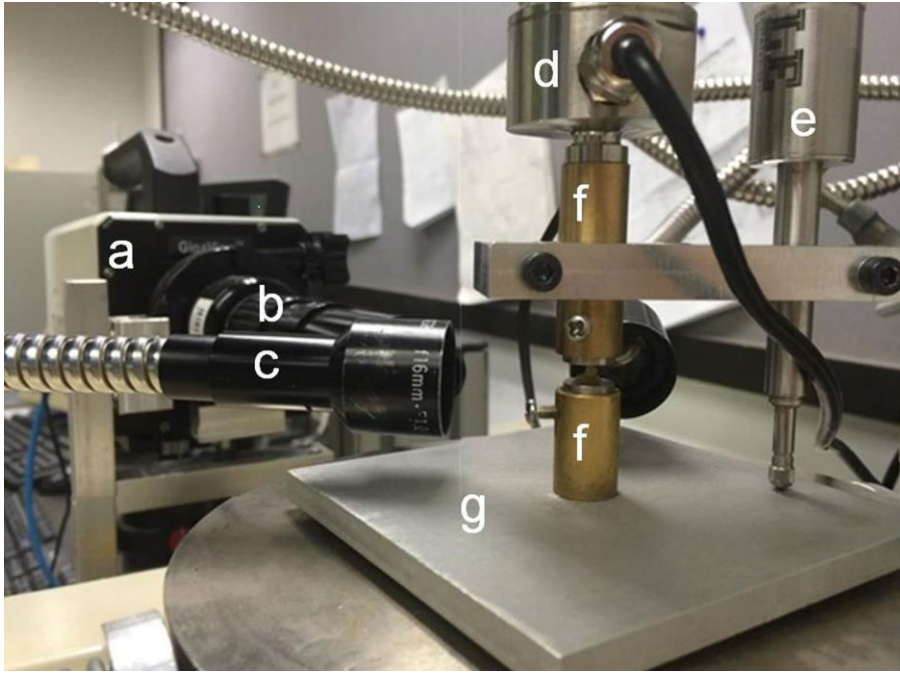
560

561 Table 2 Description of the tests.

TEST CONFIGURATION	Number of tests			
	Total	Study of Morphology		
		Tests for morphology	Initiation of the crack at the top of the particle	Not considered (no video available)
LBS -SP	90	76	8	-
LBS-CN4-BP	59	-	-	-
LBS-CN6-BP	34	-	-	-
LBS-CN4-PP	70	65	6	8
LBS-CN6-PP	65	51	-	-
LBS-CN6-PPsmall	44	30	-	-
LMS -SP	28	24	-	-
LMS-CN4-BP	39	-	-	-
LMS-CN6-BP	36	22	-	-
LMS-CN4-PP	56	51	-	-
LMS-CN6-PP	58	53	-	-
LMS-CN6-BPsmall	16	-	-	-

562

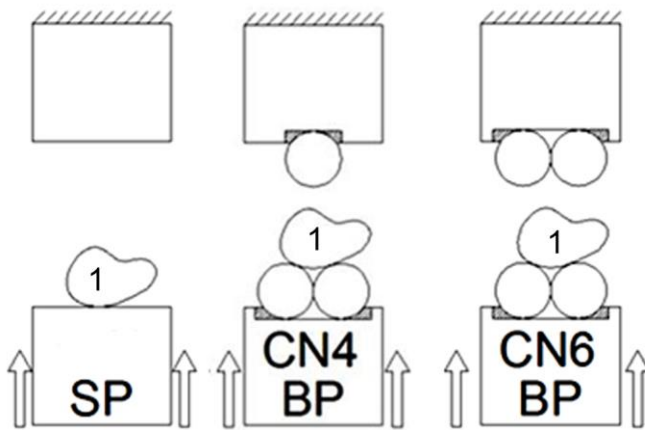
563



564

565 Fig. 1 Equipment for the multi-axial crushing tests: a) high speed camera; b) microscope lens;  
 566 c) additional lighting system with focussing lenses; d) load cell; e) LVDT; f) brass wells  
 567 containing steel mounts; g) base support resting on ball bearings.

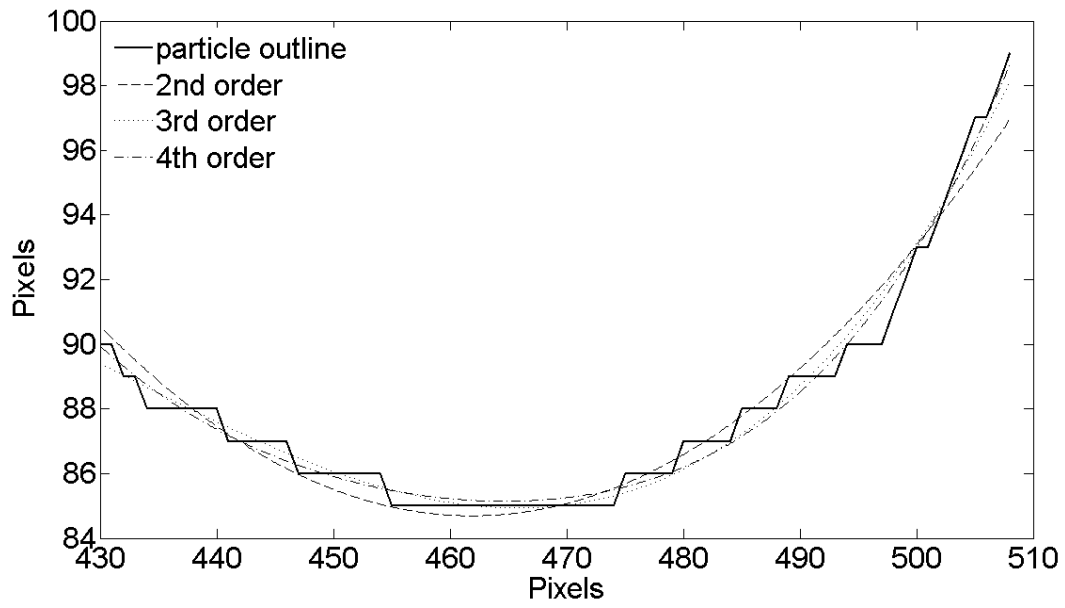
568



569

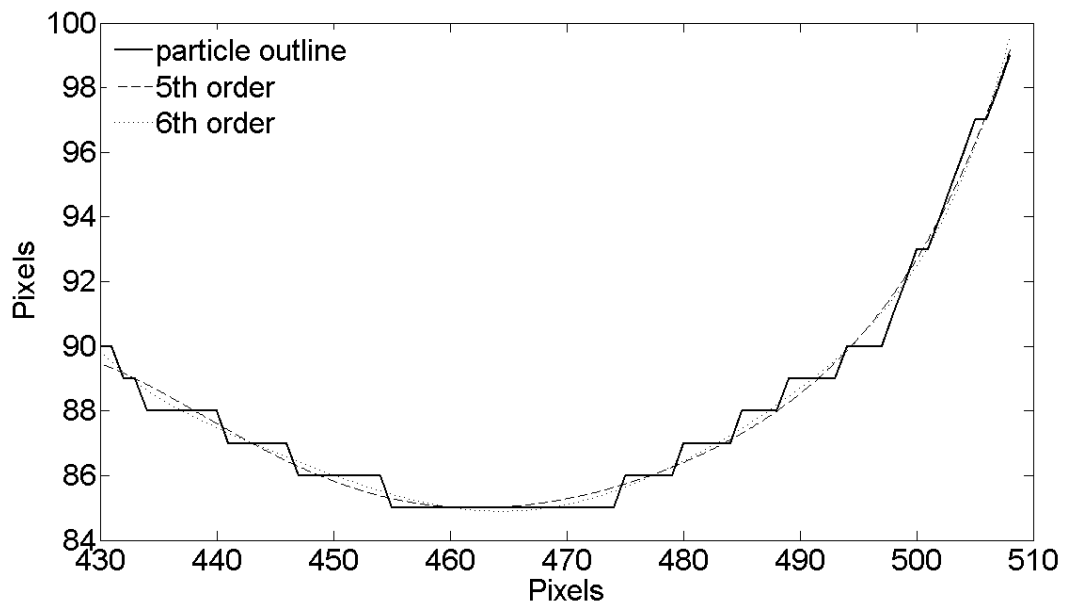
570 Fig. 2 Schematic representation of the multi-contacts crushing tests for particles tested  
 571 between hardened steel mounts (SP), between 4 steel balls (CN4-BP) and between 6 steel  
 572 balls (CN6-BP).

573



574

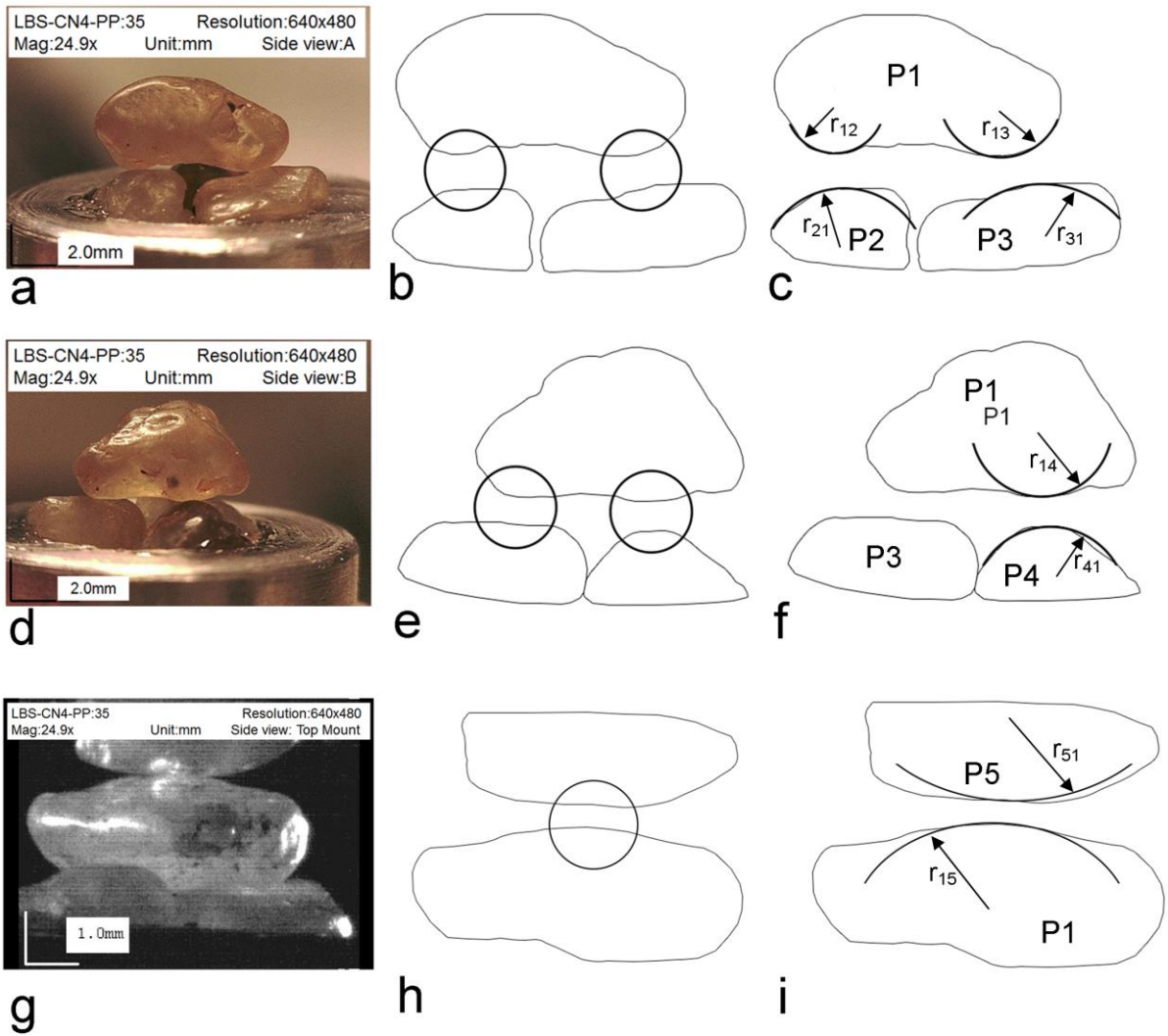
575 a)



576

577 b)

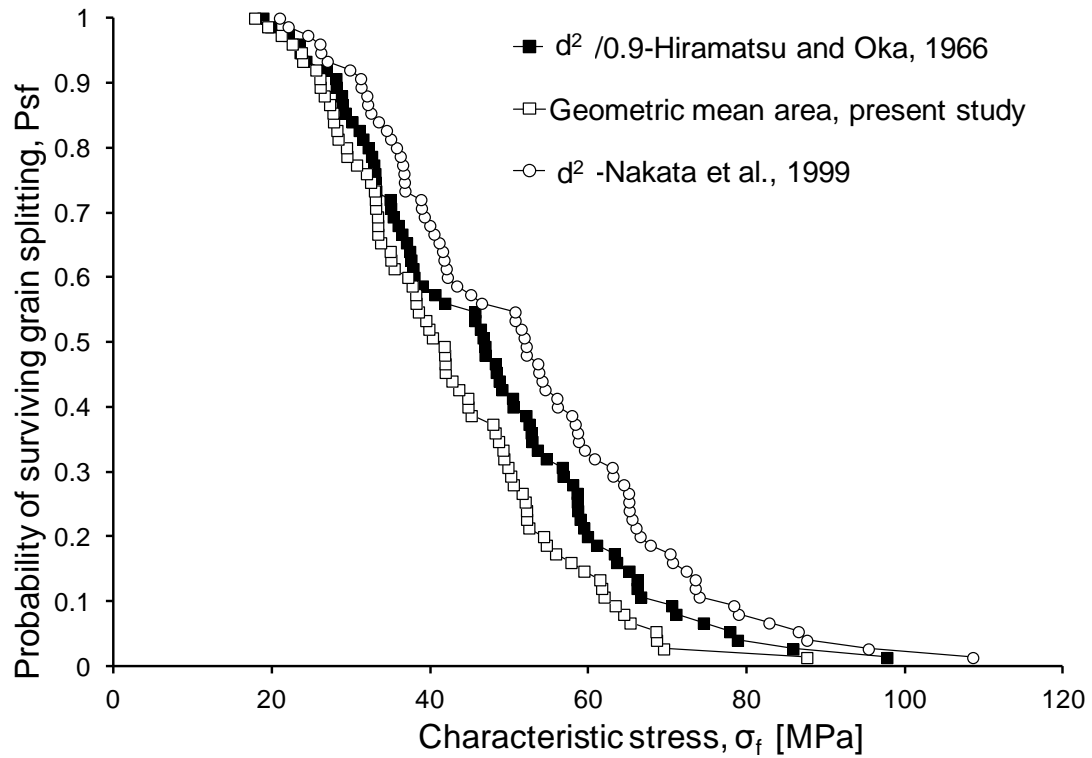
578 Fig. 3 Fitting of a particle outline by polynomial functions of different orders: a) 2<sup>nd</sup>, 3<sup>rd</sup> and  
 579 4<sup>th</sup> orders; b) 5<sup>th</sup> and 6<sup>th</sup> orders.



580

581 Fig. 4 Example of the local relative roundness parameter,  $r_{tl}$ , of test no.35, LBS-CN4-PP  
 582 based on 3 views: a) side view A of the lower mount; b) location of the contact points of side  
 583 side view A; c) definition of local radius of curvature for each contact of side view A; d) side view  
 584 B of the lower mount; e) location of the contact points of side view B; c) definition of local  
 585 radius of curvature for each contact of side view B; g) view of top mount; h) location of the  
 586 contact points at top mount; i) definition of the local radius for the contact at the top. The  
 587 arrows are indicative.

588



589

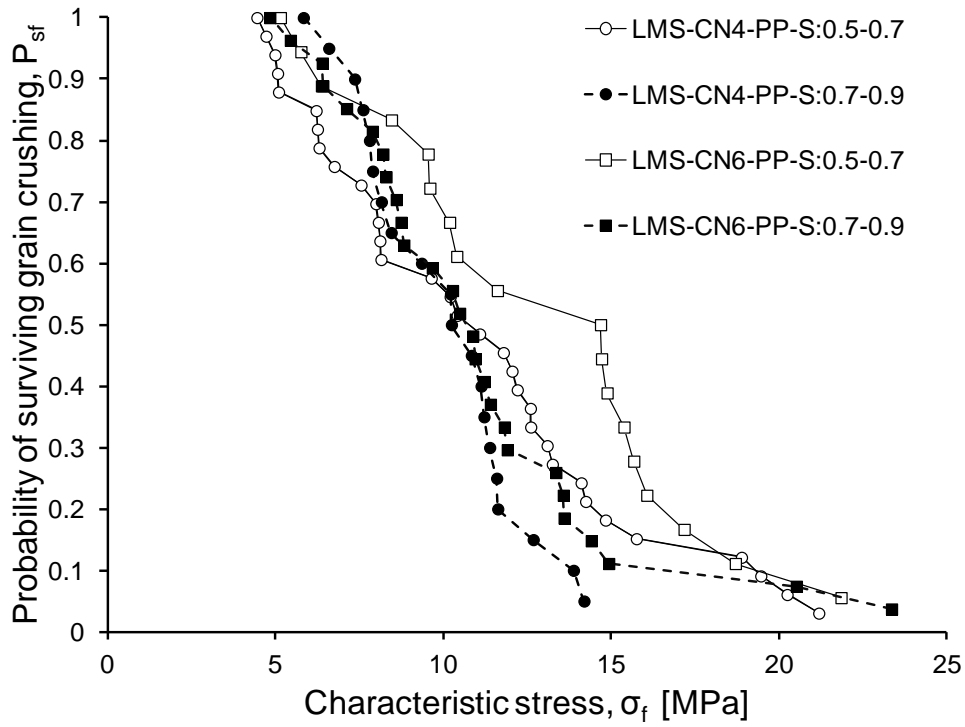
590 Fig. 5 The effect of the failure area on the strength of the LBS particles crushed between two  
 591 hardened steel mounts, i.e. LBS- SP. The geometric mean area has been adopted in this study.



592

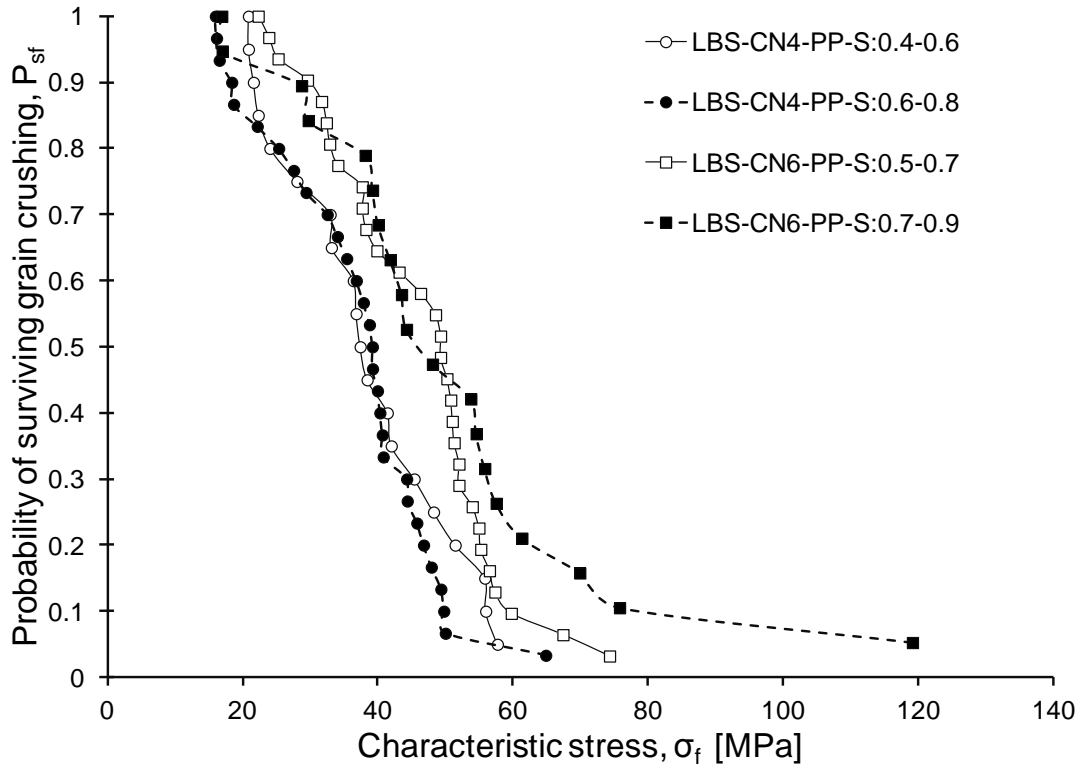
593 Fig. 6 Flat-to-flat contacts between LMS particles.





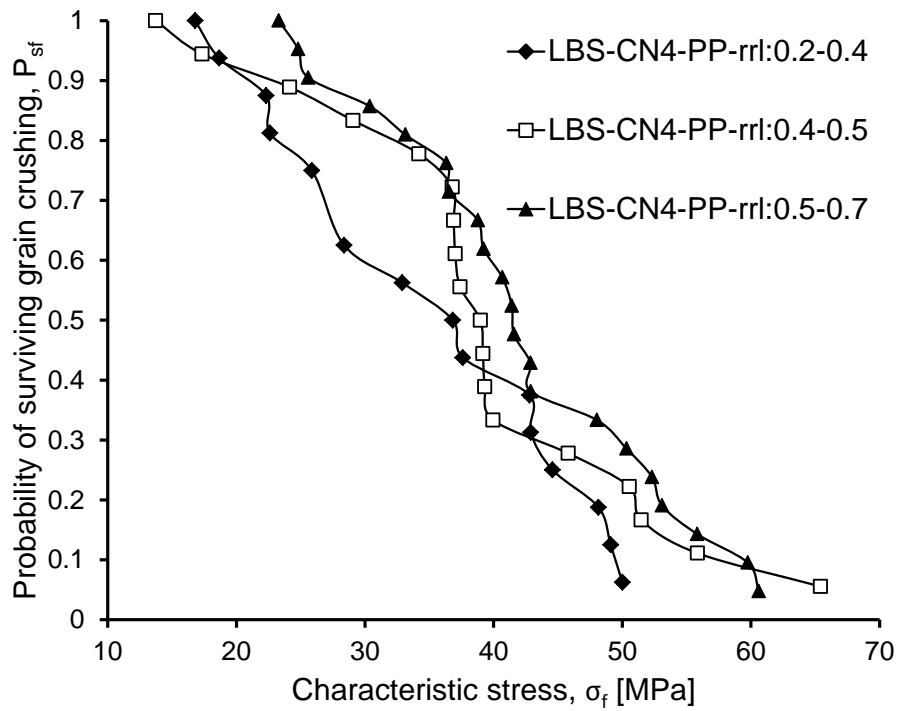
594

595 Fig. 7 The effect of sphericity on the strength of LMS particles.

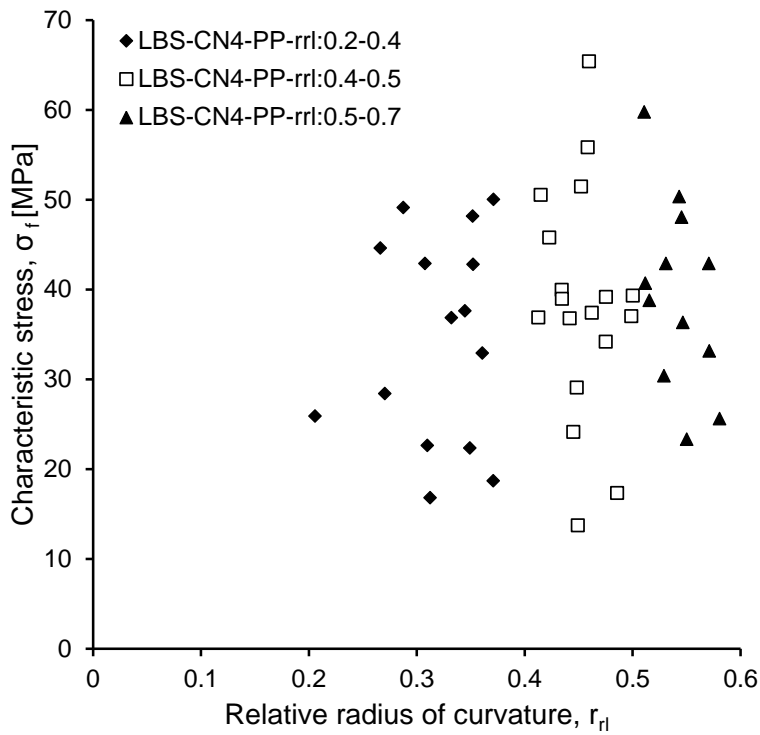


596

597 Fig. 8 The effect of sphericity on the strength of LBS particle.

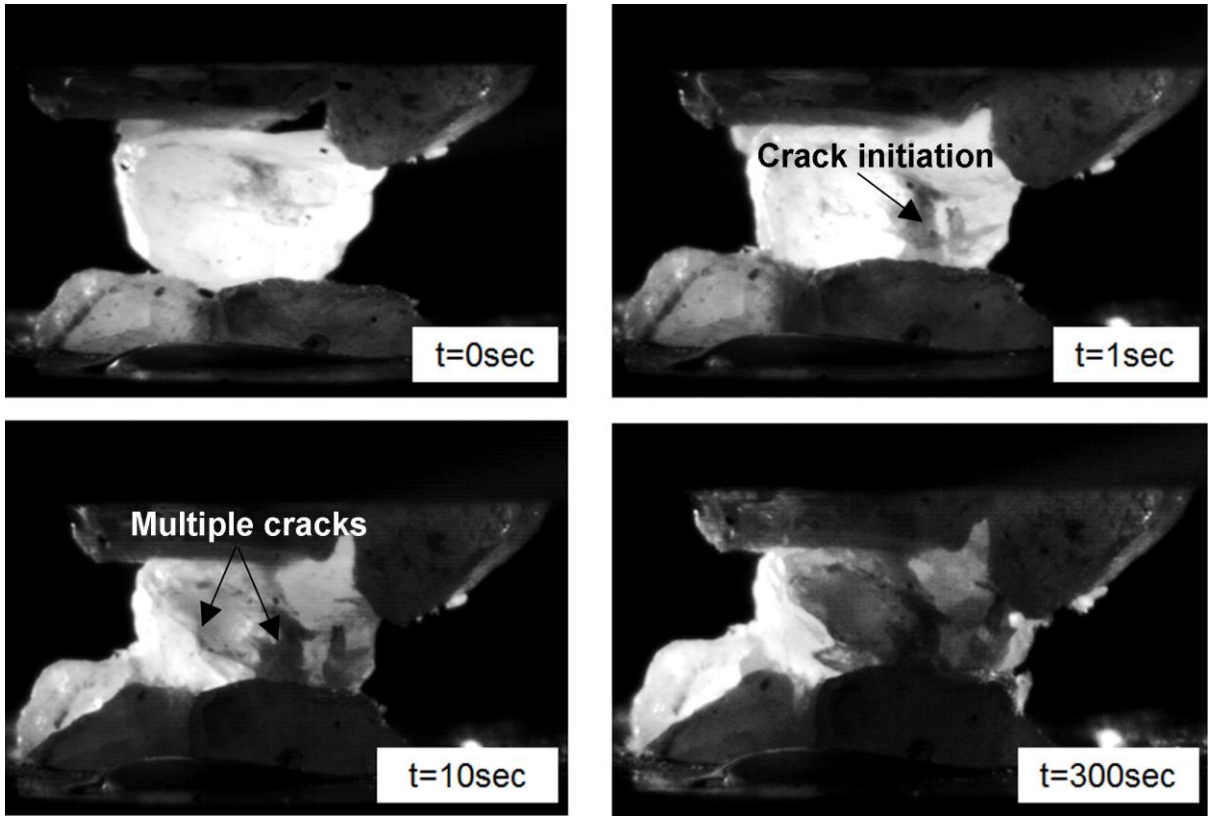


599 a)



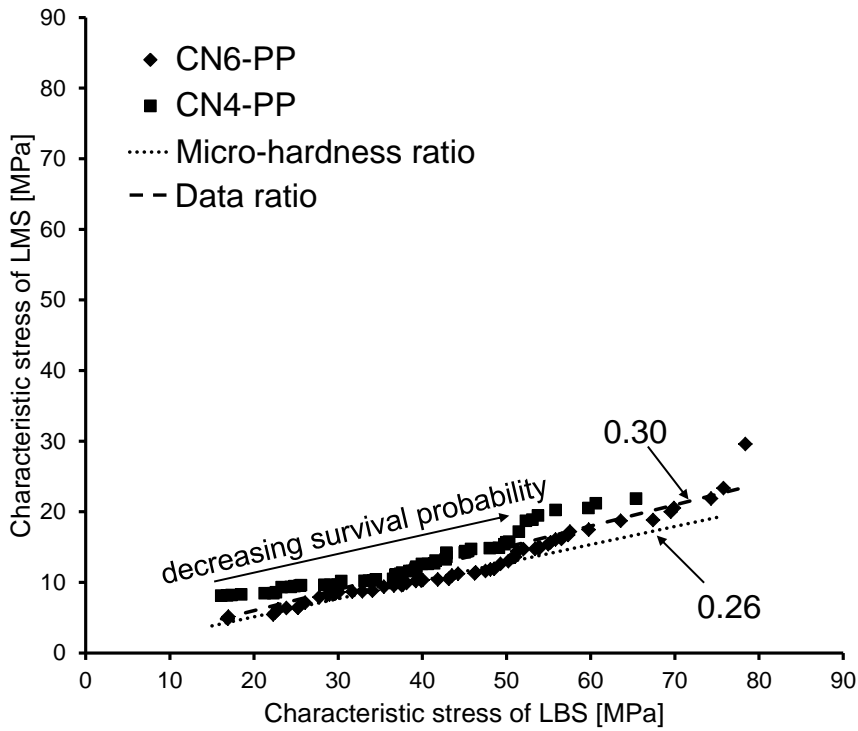
601 b)

602 Fig. 9 The effect of local roundness parameter,  $r_{ri}$ , on LBS particles: a) probability of  
 603 surviving grain crushing; b) relationship between the characteristic stress and the  $r_{ri}$ .



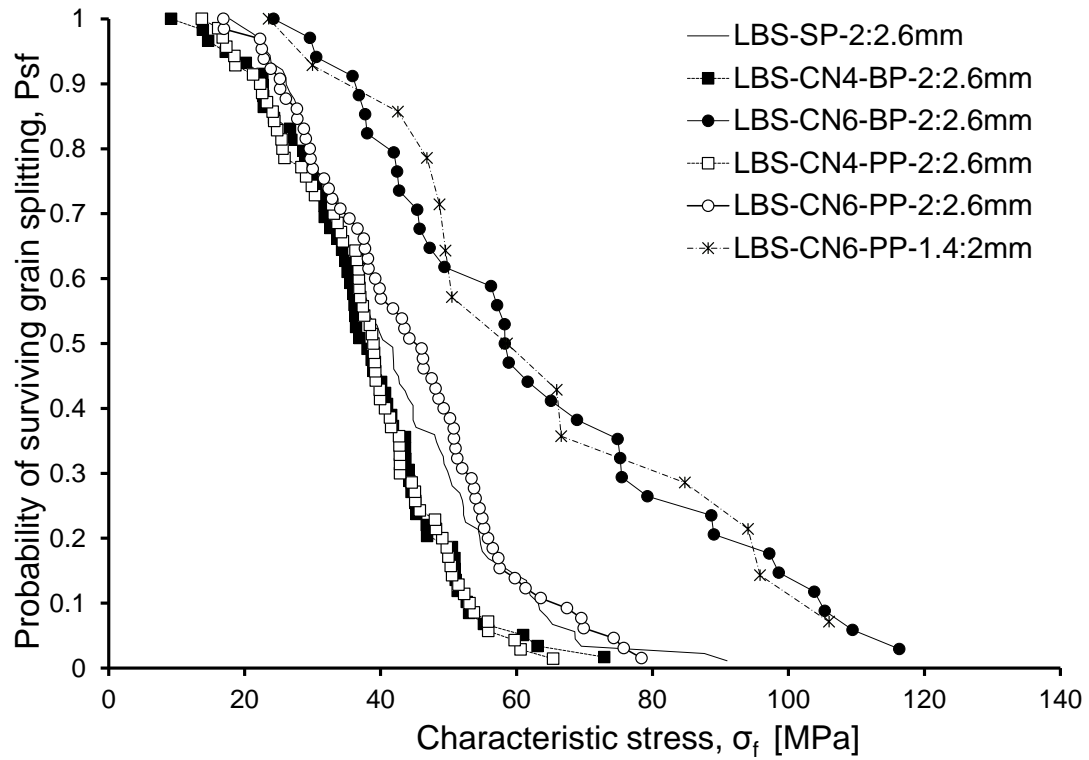
604

605 Fig.10 Example of the crushing mechanism of LMS particle tested in CN6-PP configuration.



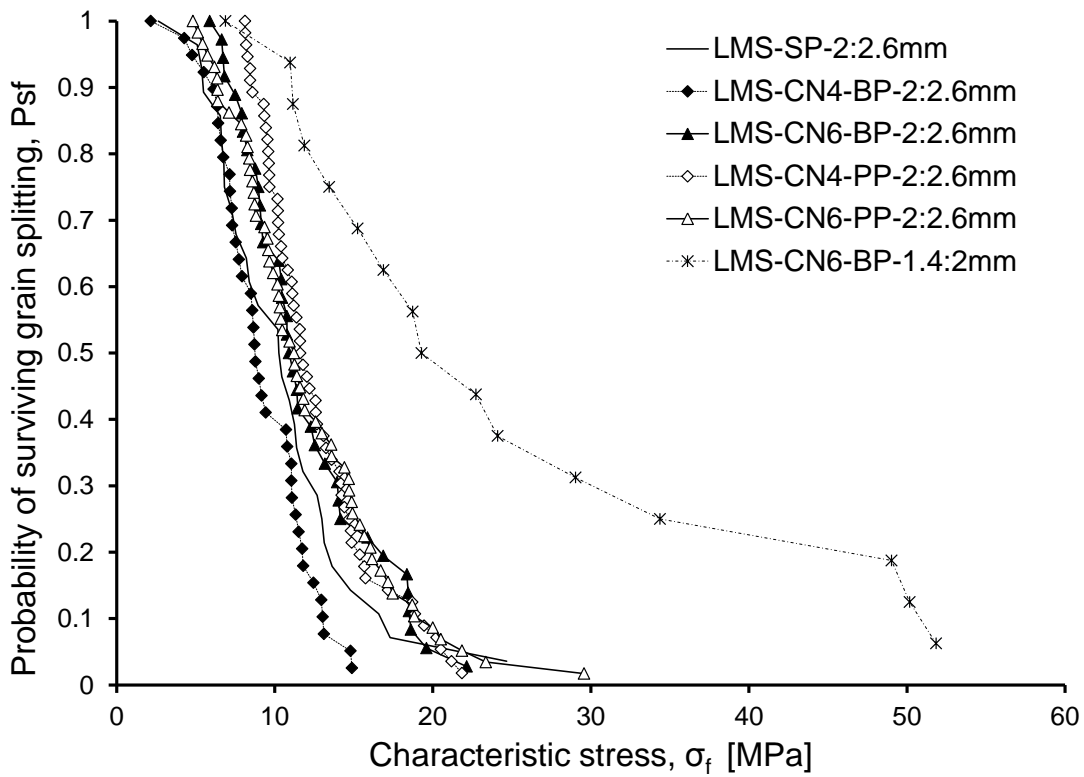
606

607 Fig. 11 Hardness relationship obtained from the characteristic stress of LBS and LMS  
 608 specimens crushed in CN4-PP and CN6-PP configurations.



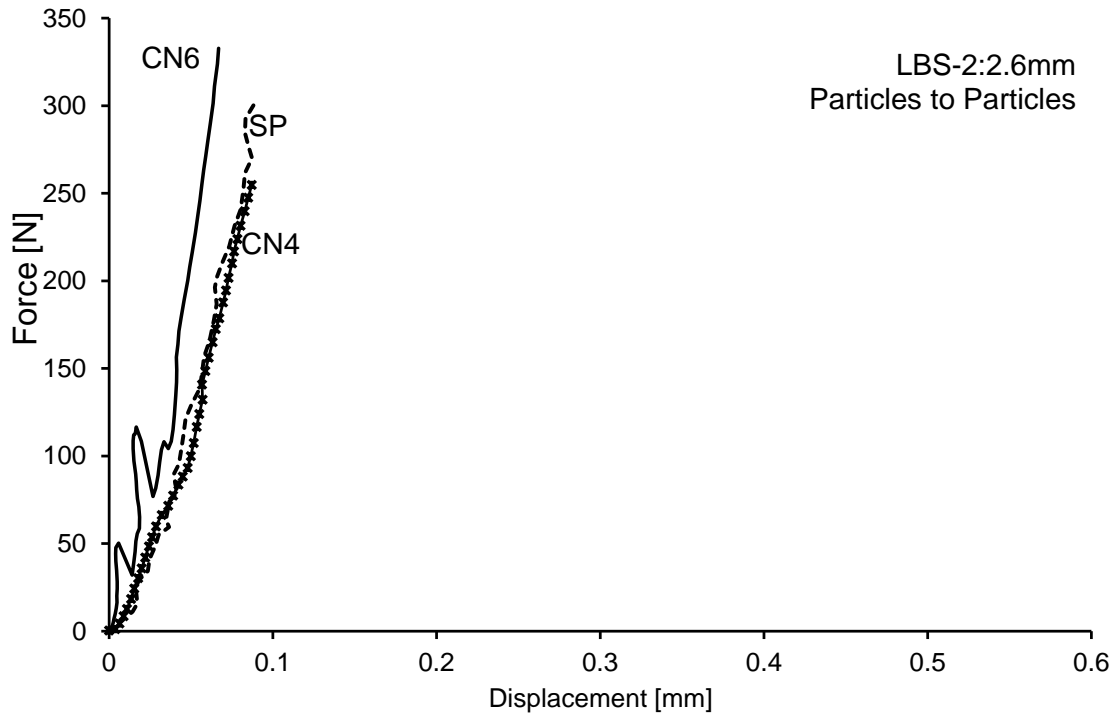
609

610 Fig. 12 Survival probability curves of LBS particles for different support particles.



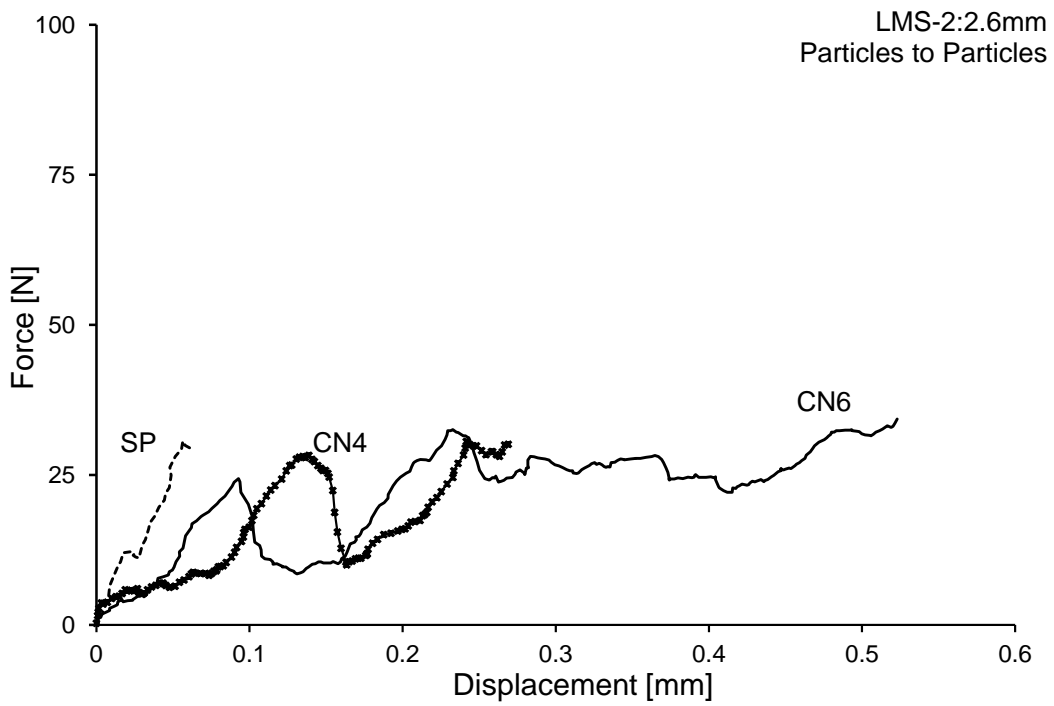
611

612 Fig. 13 Survival probability curves of LMS for different support particles.



613

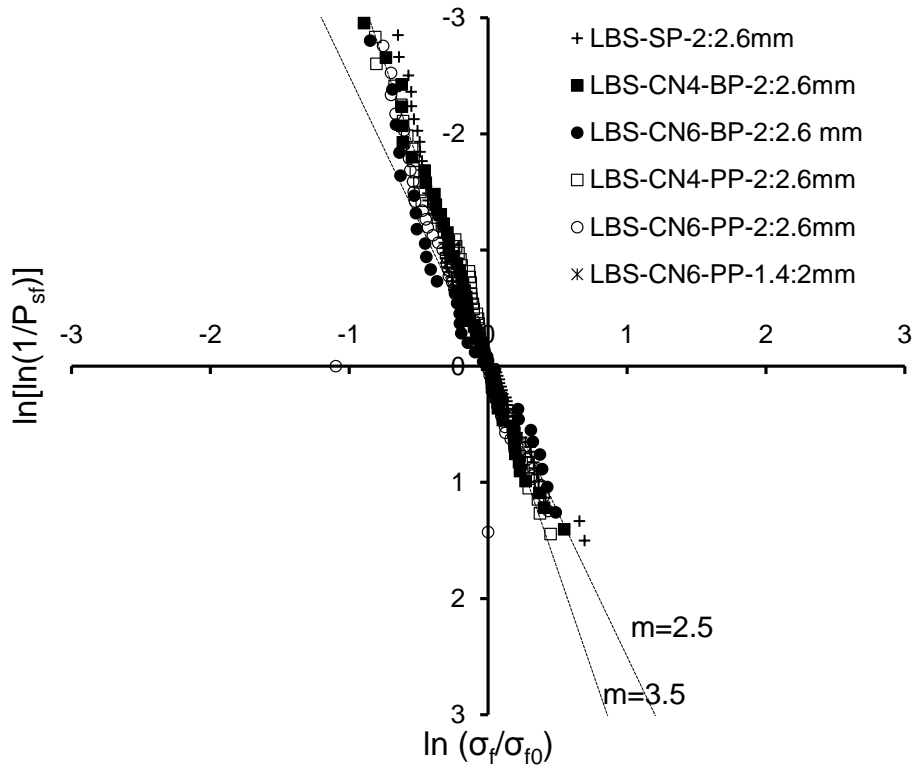
614 a)



615

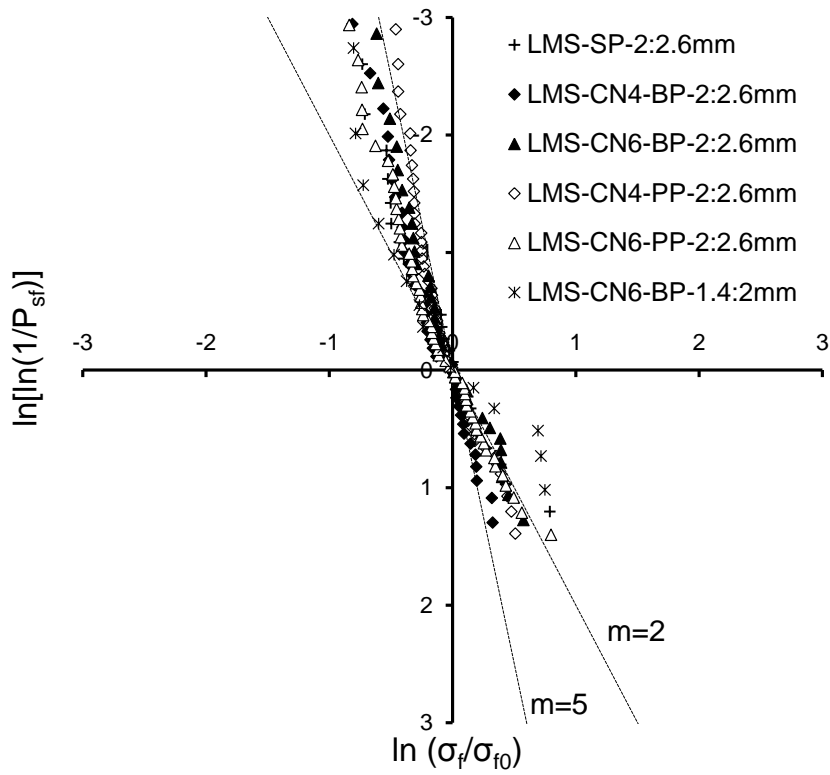
616 b)

617 Fig. 14 Force-displacement relationship of a) LBS (present study) and b) LMS (redrawn from  
 618 Todisco et al., 2015) particles.



619

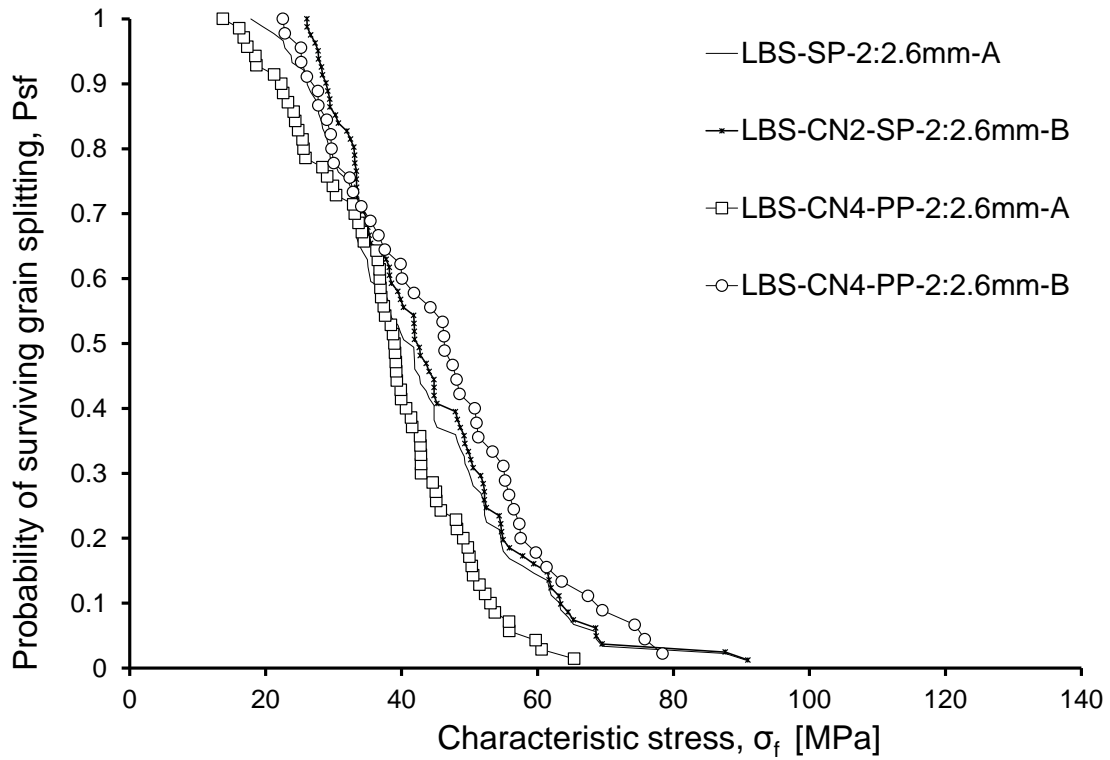
620 a)



621

622 b)

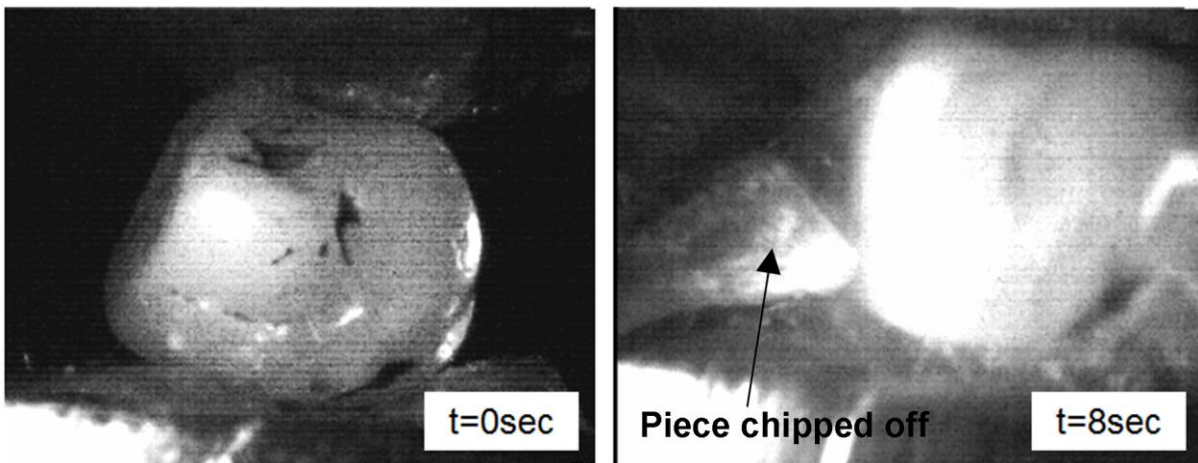
623 Fig. 15 The m-modulus of the tested sands: a) LBS specimens; b) LMS specimens.



624

625 Fig. 16 Probabilities of survival of LBS particles for which the crack initiation did not occur  
 626 near the top contact. The data refer to SP and CN4-PP configurations. (A all data, B with  
 627 failures near top contact eliminated)

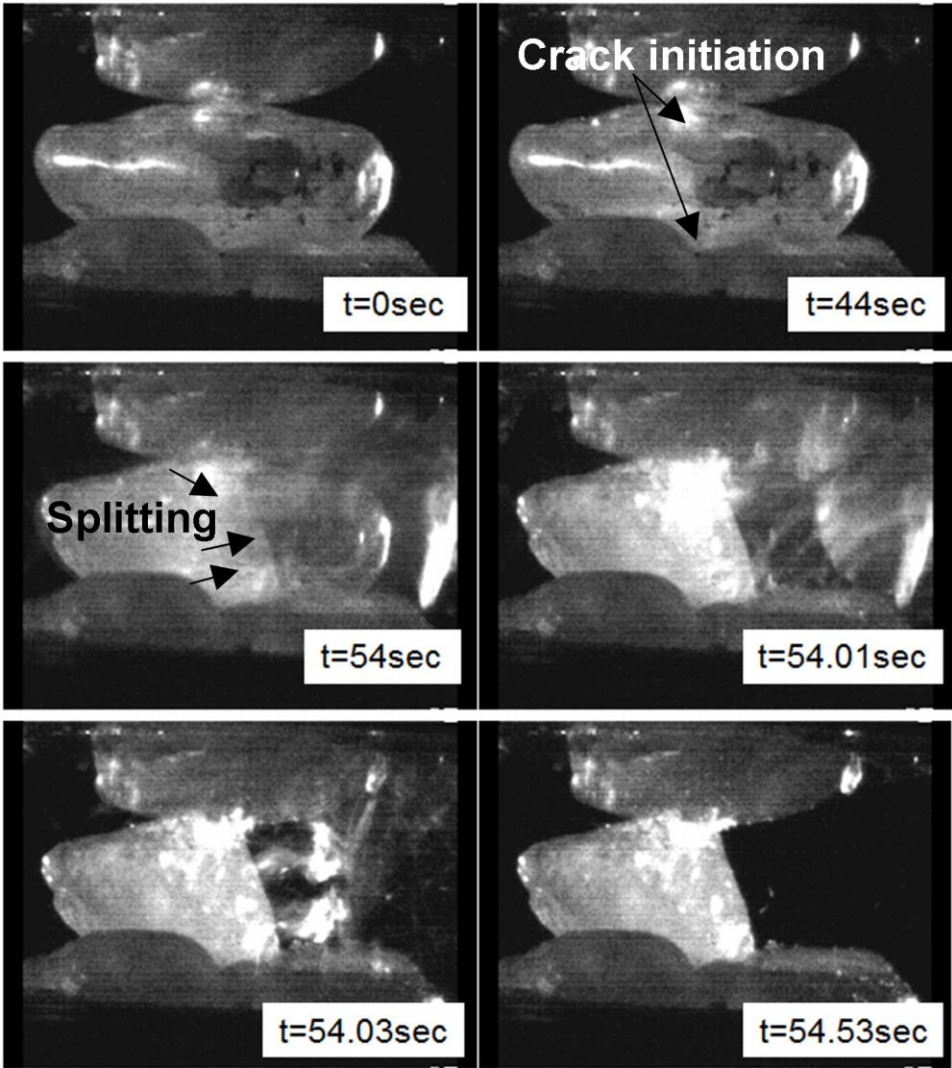
628



629

630 Fig. 17 Chipping crushing mechanism of LBS particle tested in between 4 particles.

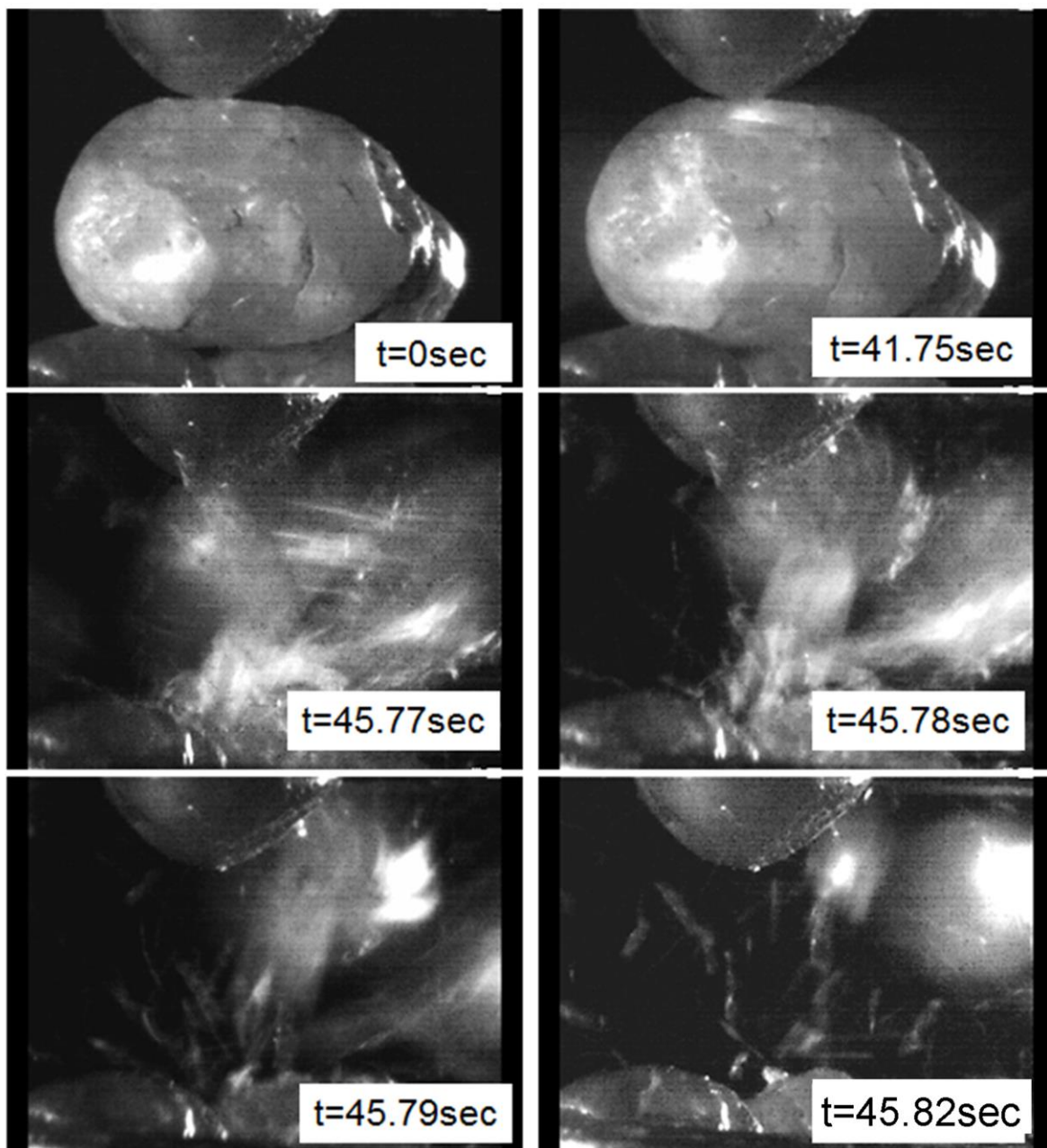
631



632

633 Fig. 18 Splitting crushing mechanism of a LBS particle tested in the CN4-PP configuration.

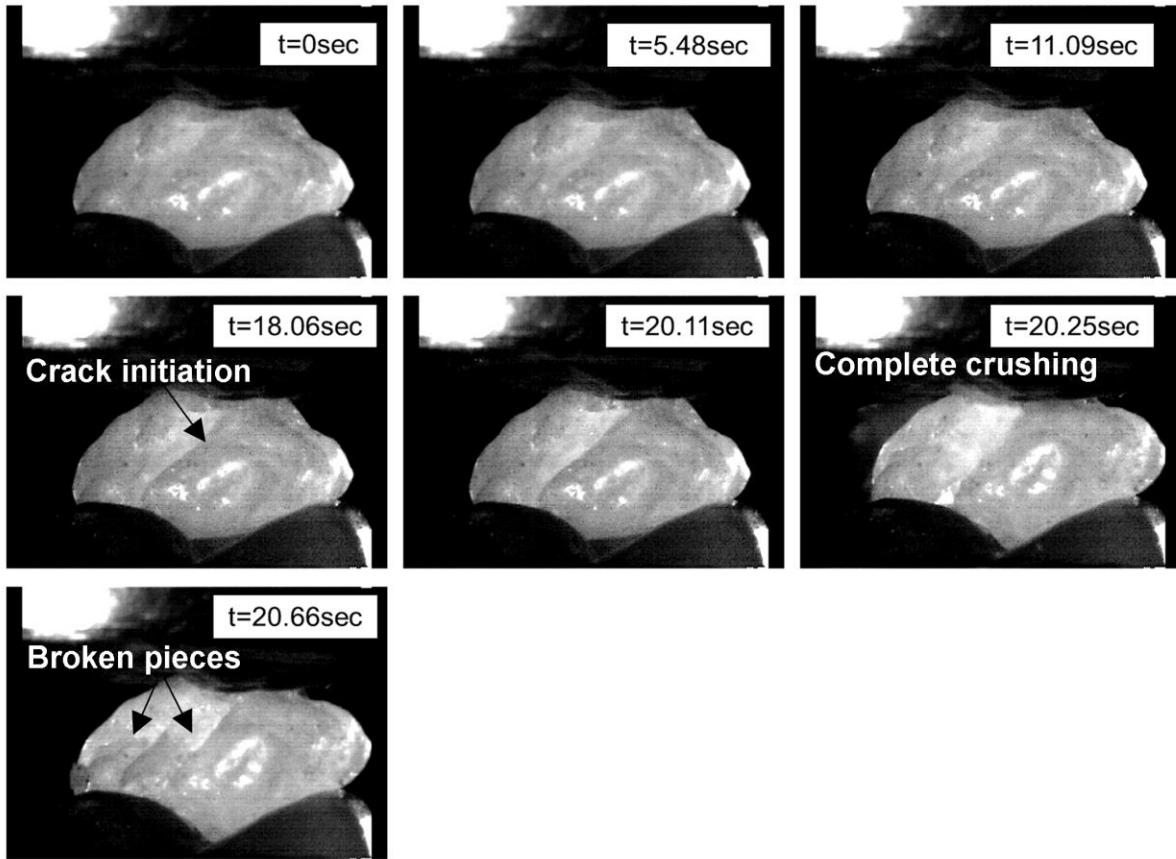




634

635 Fig. 19 Fragmentation crushing mechanism of a LBS particle crushed in between 4 particles.

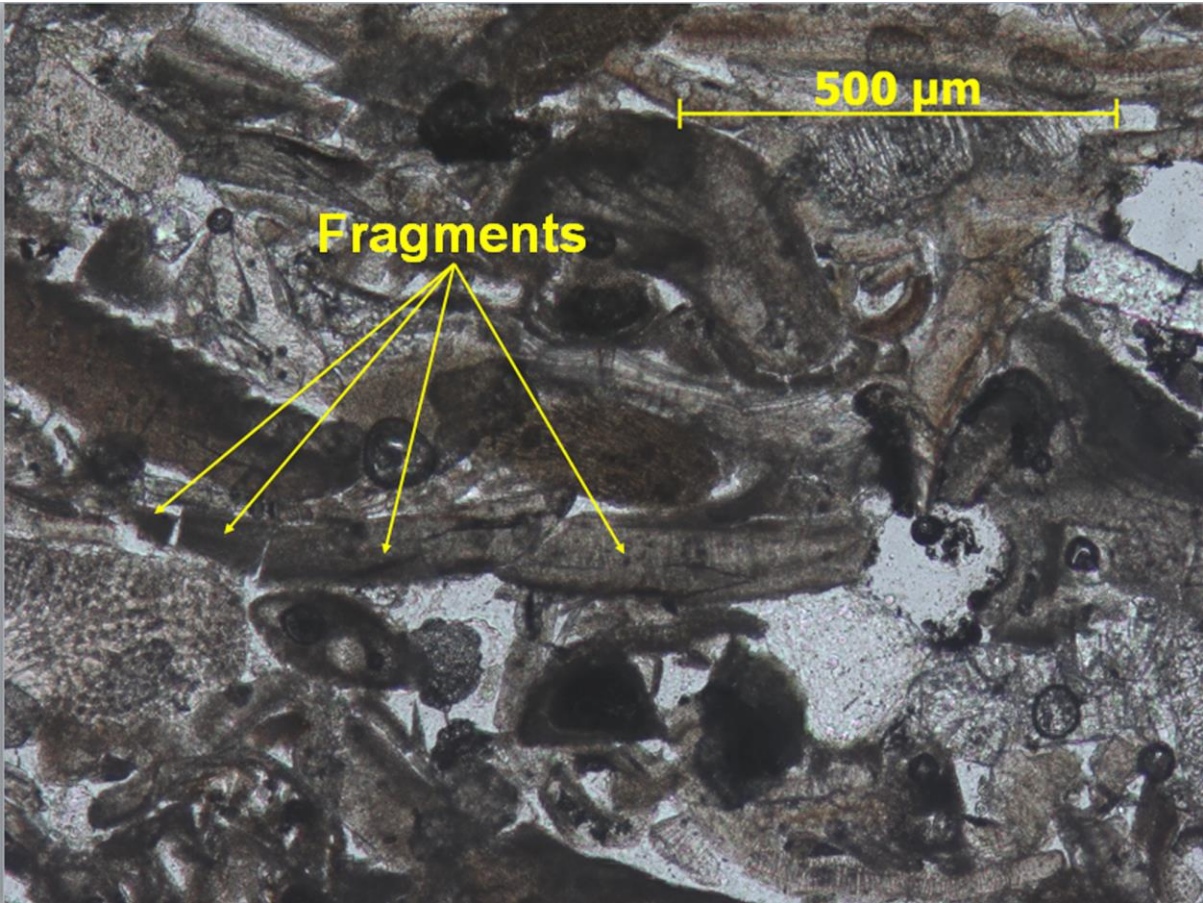
636



637

638 Fig. 20 Splitting crushing mechanism of a LBS particle tested in the CN6-PP configuration.

639



640

641 Fig. 21 Example of fragments of particle which are confined to their initial position (redrawn  
642 from Bandini and Coop, 2011).

643